Vertical moistening by AMMA mesoscale convective systems.

Georges Scialom, Yvon Lemaître

Vertical Moistening by AMMA Mesoscale Convective Systems

G. SCIALOM AND Y. LEMAÎTRE

Laboratoire Atmosphères, Milieux, Observations Spatiales, IPSL, Vélizy, France

(Manuscript received 21 April 2010, in final form 10 November 2010)

ABSTRACT

The apparent heat source Q_1 and the apparent moisture sink Q_2 are crucial parameters for precipitating systems studies because they allow for the evaluation of their contribution in water and energy transport and infer some of the mechanisms that are responsible for their evolution along their lifetime. In this paper, a new approach is proposed to estimate Q_2 budgets from radar observations within precipitating areas at the scale of the measurements, that is, either convective scale or mesoscale, depending on the selected retrieval zone. This approach relies upon a new analysis of the radar reflectivity based on the concept of the traditional velocity–azimuth display (VAD) analysis. From the following five steps, Q_2 is deduced from velocity and reflectivity fields: (i) mixing ratio retrieval using empirical relations, (ii) radial wind analysis using the VAD analysis, (iii) radar reflectivity analysis using a new analysis called reflectivity–azimuth display (RAD), (iv) retrieval of mixing ratio derivatives, and (v) Q_2 retrieval.

The originality and the main interest of the present approach with respect to previous studies rely on the fact it uses radar data alone and is based on a relatively low-cost analysis, allowing future systematic application on large datasets.

In the present paper, this analysis is described and its robustness is evaluated and illustrated on three cases observed during the African Monsoon Multidisciplinary Analyses (AMMA) special observing period (SOP) field experiment (15 June–15 September) by means of the Recherche sur les Orages et Nuages par un Système Associé de Radars Doppler (RONSARD) radar.

Results are analyzed in terms of the convective or stratiform character of observed precipitation.

1. Introduction

Convective systems of tropical or midlatitudes are thermodynamic machines in which heat and moisture, first concentrated in the lower atmospheric layers, are progressively transported to higher altitudes during the system evolution. With variable efficiency these systems transform the convective available potential energy into kinetic energy. This transformation is operated in particular by means of (i) latent heat through microphysical mechanisms, which lead to cloud and precipitating hydrometeor development; (ii) horizontal and vertical transports of water, momentum, and energy; and (iii) multiscale dynamic and thermodynamic processes, which maintain these systems.

These convective systems are often organized in lines, like squall lines, with a narrow line of convective cells to the front of the system followed by a trailing anvil composed of stratiform precipitation, or with a more circular structure. Less organized classes of convective systems also exist, which are mainly composed of stratiform rain with embedded convective cells. In tropical latitudes it is generally claimed that organized systems are responsible for about 80% of the total rain provided in these regions, and therefore they are the object of numerous studies. As an example, the main features of squall lines observed over the eastern Atlantic Ocean during the Global Atmospheric Research Program (GARP) Atlantic Tropical Experiment (GATE) were described by Zipser (1977), Zipser et al. (1981), and Houze (1977). Continental West African squall lines in the north of Ivory Coast were scrutinized for the first time in Africa by means of Doppler radars (Chong et al. 1987) during the Convection Profonde Tropicale 1981 (COPT 81) experiment. A preliminary experiment allowed squall-line description from radiosonde data in 1979 (Lemaître 1982; Lemaître and Testud 1986). North Australian systems (squall lines or stratiform clouds with embedded convection) were studied during the Down Under Doppler and Electricity Experiment (DUNDEE;

Corresponding author address: Georges Scialcom, Boulevard d'Alembert, Quartier des Garennes 11, LATMOS-IPSL-UVSQ/CNRS, 78280 Guyancourt, France.
E-mail: georges.scialom@latmos.ipsl.fr

DOI: 10.1175/2010JTECHA1486.1

Cifelli and Rutledge 1998). This study showed the dominant convective origin of rain, which was not observed in other regions. Tropical oceanic anvils between South Vietnam and Borneo were also studied by Johnson and Young (1983) during the Winter Monsoon Experiment (MONEX). Many recent studies concerning tropical convective systems use the data produced by the Tropical Rainfall Measuring mission (TRMM) satellite (Simpson et al. 1988) alone, or in synergy with related ground-based instruments during devoted field experiments, such as the South China Sea Monsoon Experiment (SCSMEX; see Johnson and Ciesielski 2002; Li et al. 2009), the North American Monsoon Experiment (NAME) over the coastal, mountainous region of northwestern Mexico (Higgins et al. 2006), or the TRMM Kwajalein Experiment (KWAJEX) in the Marshall Islands (Schumacher et al. 2008). Midlatitude squall lines and other convective systems exhibiting structures similar as those of tropical systems were also the subject of numerous studies (see, e.g., Maddox 1980, 1983; Smull and Houze 1985; Heymsfield and Schotz 1985; Gallus and Johnson 1991; Tao et al. 1993; Lin and Johnson 1994).

These studies reveal that convective systems present variable structures and efficiencies in their production of rain. This variability depends on their environment, which is more or less favorable to their initiation, development, and decay, and leads to numerous types of systems. The study of these systems concerns their dynamics, thermodynamics, microphysics, and heat and moisture exchanges with their environment.

Heat and moisture budgets are often evaluated using the concept of Q_1 and Q_2 (apparent heat source and apparent moisture sink, respectively) introduced by Yanai et al. (1973). In an elegant way this concept, along with the use of a cloud model, provides the macroscopic properties of cloud clusters with cumulus ensemble exchanging mass, heat, liquid water, and moisture with the environment through entrainment and detrainment. It reveals how the environmental air is heated and moistened by the cumulus convection, and it quantifies the impact of underlying processes.

Numerous analyses of convective systems in terms of Q_1 and Q_2 followed this pioneering work. These studies, focusing on case studies and large scales, either are based on conceptual models (Houze 1982), numerical models (Tao et al. 1993), various datasets alone on Winter MONEX (Johnson and Young 1983), on DUNDEE (Cifelli and Rutledge 1998), or on Tropical Ocean–Global Atmosphere Coupled Ocean Atmosphere Response Experiment (TOGA COARE) (Yang and Smith 2000), or they are combined with conceptual or numerical modeling [Chong and Hauser 1990; Lafore et al. (1988) on COPT81]. The onset of the Australian summer monsoon was also studied in this way (Hung and Yanai 2004), and its year-to-year variability was determined by using, in particular, data from the Australian Monsoon Experiment (AMEX). Latent heating of rainfall in the vicinity of the Himalayas was studied during the three years from 2000 to 2002, thanks to the precipitation radar (PR) of the TRMM satellite overpasses above an area covered by radiosondes (Magagi and Barros 2004).

Other field programs were conducted over various tropical locations in order to provide observational validations for numerical models and TRMM algorithms. This is the case for the TRMM Large Scale Biosphere–Atmosphere Experiment in Amazonia (TRMM-LBA, Silva Dias et al. 2002), the Tropical Eastern Pacific Process Study (TEPPS; Yuter and Houze 2000), and the East Pacific Investigation of Climate Processes in the Coupled Ocean–Atmosphere System (EPIC; Raymond et al. 2004).

Latent heating profiles were determined using a new algorithm applied to TRMM PR data over the TOGA COARE region, and extended to other tropical oceanic regions [GATE, SCSMEX, and KWAJEX; see Shige et al. (2004, 2007, 2008, 2009)].

Recently the context of insufficient precipitation over the west African Sahel region for the past 40 yr has motivated new studies and led a large part of the international scientific community to organize the African Monsoon Multidisciplinary Analysis (AMMA) (Redelsperger et al. 2006) and National Aeronautic and Space Administration (NASA) AMMA (NAMMA) programs (Zipser et al. 2009). The AMMA program presented a unique opportunity to gather an important dataset at several scales, allowing multiscale studies of Q_1 and Q_2 to be performed using various strategies based on either radiosonde observations, delineating a quadrilateral contained within a ~1000-km circular region; Doppler radar observations, using a 1D microphysical retrieval model; or numerical simulations.

During the special observing period (SOP; 15 June–15 September 2006) of AMMA several Doppler radars were sampling precipitation systems over north Benin and south Niger, including the Recherche sur les Orages et Nuages par un Système Associé de Radars Doppler (RONSARD) radar, which recently had been equipped with dual-polarization capability (Scialom et al. 2009).

In this context this paper addresses the contribution of the convective scale and small mesoscale in the water cycle of the African monsoon. It proposes a new approach for estimating the vertical moistening distributions within the mesoscale convective systems observed in the African monsoon. The present approach derives the apparent moisture sink Q_2 from Doppler radar data alone by a new method that exploits the main two measured parameters—radar reflectivity and velocity field.

Performing this estimate at 30–100-km scale, which is thus at smaller scales than those in previous studies, allows for a straightforward partition of the moisture budget between convective and stratiform components. The vertical profile of vertical velocity and terminal fall velocity obtained by the velocity–azimuth display (VAD) analysis and the horizontal pattern of the reflectivity field are used to perform this partition.

This paper exploits the data from the RONSARD radar that was implemented during AMMA about 18 km from Djougou in northern Benin.

Section 2 is devoted to the methodology used, with a preliminary point concerning RONSARD radar preprocessing. As will be shown, the method needs a prior estimate of the wind and its derivatives and the reflectivity and its time and space derivatives.

Then, in section 3, three examples of Q_2 estimates for convective systems observed in northern Benin by the RONSARD radar during the AMMA SOP are presented. These examples are representative of convective systems during the monsoon pre-onset, the monsoon onset, and the monsoon decay, respectively. Section 4 analyses the radar-derived Q_2 in light of the previous studies performed at larger scales, and perspectives of this work are given.

2. Q_2 retrieval from radar measurements

a. RONSARD radar preprocessing

Data were corrected by applying classical preprocessing plus correction for attenuation.

1) CLASSICAL PREPROCESSING

The radar performed plan position indicator (PPI) volume scans at maximum ranges of 102.8 or 205.6 km, with gate widths of 100 or 200 m, respectively, depending on the operating mode. Within each gate several polarimetric variables are recorded, in particular, Z_{HH}, Z_{VV}, V_{HH}, V_{VV}, and Φ_{DP} (see Scialom et al. 2009 for details). Respectively, Z_{HH} and Z_{VV} are the copolar reflectivities at horizontal and vertical polarizations, V_{HH} and V_{VV} are the velocities at horizontal and vertical polarizations, and Φ_{DP} is the differential phase shift.

Low signal-to-noise ratio (SNR) signals are characterized by low reflectivities and incoherent velocities. Second-trip echoes are also characterized by incoherent velocities, but reflectivities may be high.

Thus, noisy measurements and second-trip echoes were eliminated by using incoherence in the Doppler velocity found in a comparison between V_{HH} and V_{VV}. These two parameters should be equal in gates containing meteorological signals, but are different when there is either noise or a second-trip echo. Thus, gates with $|V_{HH} - V_{VV}|$ greater than 0.5 m s^{-1} are eliminated.

Ground clutter was eliminated by comparison with a digital terrain model. Reflectivity was calibrated by comparing with reflectivity retrieved from disdrometers and from the TRMM PR data.

A specific algorithm was developed for dealiasing Doppler velocities. This algorithm operates by continuity of the wind on a radial and in an area swept by the azimuth and/or the elevation. In addition to this systematic data processing, specific corrections were applied to the azimuth.

Finally, the whole processing, including intercomparison with other types of instruments, allowed for the quality control of the dataset.

2) ZPHI APPLICATION

Attenuation and differential attenuation were corrected using the ZPHI algorithm (Testud et al. 2000). Using the polarimetric data, in particular, Z_{HH}, Z_{VV}, and Φ_{DP}, the algorithm corrects for the attenuation of reflectivity by rain. ZPHI also allows for the various types of precipitation to be distinguished while performing hydrometeor classification. The various polarimetric variables processed with ZPHI thus allow for the exploration of the microphysical structure of observations.

Rainfall rates and drop size distribution (DSD) characteristics, in particular, N_0^*, are also available.

The correction for attenuation is based on the linearity between attenuation and Φ_{DP}. The algorithm possesses an additional internal calibration check that corrects for possible residual calibration errors (Le Bouar et al. 2001). Additionally, the sensitivity of the scheme to the variability of the DSD is reduced because the ray is partitioned into several segments that are independently processed, instead of being considered as a whole. The quality of the retrieved attenuation profile for Z_{HH} is checked through comparison between retrieved and measured Φ_{DP}.

b. Principle of Q_2 retrieval

The apparent moisture sink Q_2 is generally defined as

$$Q_2 = \left\langle -\left(\frac{L}{c_p}\right) dq_v/dt \right\rangle, \quad (1)$$

where L and c_p are the latent heat for vaporization of water and the specific heat at constant pressure for water, respectively, and angled brackets indicate averaging over time and space. The Lagrangian time derivative of

the water vapor mixing ratio dq_v/dt is derived from the continuity equation

$$\frac{\partial q_v}{\partial t} + (\mathbf{V}\cdot\nabla)q_v = e - c, \tag{2}$$

where $\mathbf{V}(u, v, w)$ is the 3D wind velocity vector. The first and second terms on the left-hand side of Eq. (2) are the Eulerian time derivative and advection terms, respectively. The right-hand-side term represents the local rate of condensation c and evaporation e.

Generally, Q_2 is quantified from radiosondes using humidity and wind measurements.

The continuity equations for precipitation (liquid or ice) and cloud water contents read

$$\frac{\partial q_p}{\partial t} + (\mathbf{V}\cdot\nabla)q_p + \left[\frac{1}{\rho}\frac{\partial(\rho q_p V_F)}{\partial z}\right] = k - e + a, \tag{3}$$

$$\frac{\partial q_c}{\partial t} + (\mathbf{V}\cdot\nabla)q_c = c - k - a, \tag{4}$$

where q_c and q_p are mixing ratios for cloud water and precipitation, respectively; k is the collection efficiency; a is the autoconversion coefficient between cloud and rain; and V_F is the terminal fall velocity of hydrometeors.

Adding (3) and (4) leads to the continuity equation for the total (either liquid or ice) mixing ratio q_{tot}:

$$q_{\text{tot}} = q_p + q_c, \tag{5}$$

$$\frac{\partial q_{\text{tot}}}{\partial t} + (\mathbf{V}\cdot\nabla)q_{\text{tot}} + \left[\frac{1}{\rho}\frac{\partial(\rho q_p V_F)}{\partial z}\right] = c - e. \tag{6}$$

In Eq. (6), the mean V_F term can be expressed in terms of q_{tot}, with a zero V_F for cloud particles, and a greater than zero for precipitation. This allows for the rewriting of Eq. (6) to the more general form,

$$\frac{\partial q_{\text{tot}}}{\partial t} + (\mathbf{V}\cdot\nabla)q_{\text{tot}} + \left[\frac{1}{\rho}\frac{\partial(\rho q_{\text{tot}} V_F)}{\partial z}\right] = c - e. \tag{7}$$

Comparing Eqs. (7), (1), and (2) shows that Q_2 can also be derived from winds and total (either ice or water) content q_{tot} measurements by averaging Eq. (7) and changing its sign.

In Eq. (7), the left-hand-side terms are the temporal evolution term, advection term, and terminal velocity term, respectively.

It is thus necessary to retrieve q_{tot}; its derivatives $\partial q_{\text{tot}}/\partial x$, $\partial q_{\text{tot}}/\partial y$, $\partial q_{\text{tot}}/\partial z$, and $\partial q_{\text{tot}}/\partial t$; the wind components u, v, and w; and the terminal fall velocity V_F.

Finally, the retrieval of Q_2 from radar data can be made through the following four steps described below.

1) Q_{TOT} RETRIEVAL

The term q_{tot} can be empirically related to the radar reflectivity η (mm^6 m^{-3})

$$q_{\text{tot}} = A\eta^b, \tag{8}$$

where A and b depends on hydrometeor type.

Note that radars generally provide the reflectivity factor Z (dBZ) related to the reflectivity η by the relation $\eta = 10^{0.1Z}$. Thus, the reflectivity factor must be converted into reflectivity before using Eq. (8).

The C-band radars like RONSARD measure a signal resulting from precipitating particles, but also cloud particles. Within precipitation, because the signal is strong, the radar is sensitive enough to measure precipitation plus the cloud signal present in the same volume. This is not the case in cloudy areas with no precipitation in which the radar is sensitive above −12 dBZ at 1-km distance. In that case, some signal can be lost. This case is not, however, likely to occur within the strong precipitation encountered here.

2) Q_{TOT} DERIVATIVES RETRIEVAL

Differentiating Eq. (8) with respect to x yields

$$\partial q_{\text{tot}}/\partial x = bA\eta^{b-1}\partial\eta/\partial x. \tag{9}$$

Similar expressions are obtained for $\partial q_{\text{tot}}/\partial y$, $\partial q_{\text{tot}}/\partial z$ and $\partial q_{\text{tot}}/\partial t$ by differentiating Eq. (8) with respect to y, z, and t, respectively.

Thus, derivatives of the radar reflectivity η are needed and obtained using the particular procedure described in the following section 2c.

3) WIND AND V_F RETRIEVAL

The quantities u, v, w, and V_F are straightforwardly deduced by the classical VAD analysis of the radar radial wind (see section 2c).

4) Q_2 RETRIEVAL

Finally, for each altitude, Q_2 can be written as

$$\begin{aligned} Q_2 &= (L/c_p)\langle dq_p/dt\rangle \\ &= (L/c_p)[\langle\partial q_p/\partial t\rangle + \langle u\rangle\langle\partial q_p/\partial x\rangle + \langle v\rangle\langle\partial q_p/\partial y\rangle] \\ &\quad + \langle w\rangle\langle\partial q_p/\partial z\rangle + V_F\langle\partial q_p/\partial z\rangle \end{aligned} \tag{10}$$

Each term like $\langle u\rangle$ (or $\langle\partial q_p/\partial x\rangle$) is the sum of a term $\langle u_0\rangle$ (or $\langle\partial q_{0\text{p}}/\partial x\rangle$) retrieved by the least squares process described hereafter and a residual term $\langle\text{u}\rangle$ (or $\langle\partial q_p'/\partial x\rangle$) that is close to zero through this process. Thus, in an expression like $\langle u\rangle\langle\partial q_p/\partial x\rangle$, which can be written as

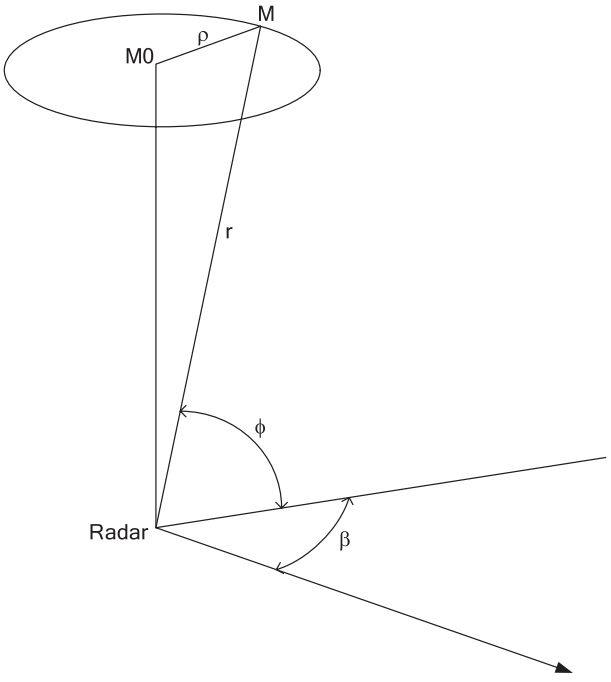

FIG. 1. Geometry of the radar observations in conical mode.

$\langle u_0\rangle\langle\partial q_{0p}/\partial x\rangle + \langle u'\rangle\langle\partial q_{0p}/\partial x\rangle + \langle u_0\rangle\langle\partial q'_p/\partial x\rangle + \langle u'\rangle\langle\partial q'_p/\partial x\rangle$, only the main term (the first one) should be retained. The second and third terms (which are of the first order with respect to the main term) and the fourth one (which is of the second order, and is thus even lower) should be neglected.

The four-step process previously presented is practically realized as follows: steps 1 and 3 are simultaneously performed (i.e., the retrieval of V, η, their derivatives, and q_{tot}), followed by step 2 (i.e., the retrieval of q_{tot} derivatives), and finally step 4 (with Q_2 calculation).

As indicated previously, step 2 highlights the need for the retrieval of mean values of η and its derivatives. This is done using a new analysis reflectivity–azimuth display (RAD), which is similar to the VAD analysis described in the next subsection.

c. *Detailed description of the method for wind and reflectivity*

Radar data processed in the method are organized in the natural geometry of conical scans swept by the antenna at increasing elevation ϕ.

For each elevation, a point $M = (x, y, z_0)$ at altitude z_0 describes a circle with radius ρ about the point M_0 (0, 0, z_0) at the radar vertical z_0 (Fig. 1). Thus,

$$\rho = r\cos\phi \quad \text{and} \quad z_0 = r\sin\phi, \tag{11}$$

where r is the radar range gate at azimuth β and elevation ϕ. Thus, M can also be defined by its polar coordinates (r, β, ϕ).

1) RECALL OF THE WIND COMPONENTS AND WIND DERIVATIVES RETRIEVAL

In the VAD analysis of the wind, the horizontal wind components u and v are assumed to vary linearly along the horizontal coordinates (Browning and Wexler 1968; Bréger 1977; Matejka and Srivastava 1981) in the considered domain:

$$u = u_0 + x\,\partial u/\partial x + y\,\partial u/\partial y, \tag{12}$$

$$v = v_0 + x\,\partial v/\partial x + y\,\partial v/\partial y, \tag{13}$$

where u_0 and v_0 are taken at M_0. The measured radial wind V_r is the projection onto the line radar–M of the real wind, that is, the sum of the horizontal air wind speed V_h and the terminal fall velocity V_F plus the vertical air wind w. Thus, V_r at a given elevation can be expressed as a function of r, β, and ϕ as

$$V_r = -V_h\cos(\beta - \beta_0)\cos\phi + (w + V_F)\sin\phi. \tag{14}$$

It can be shown that the linearity hypothesis for u and v implies that the radial velocity obtained at a particular radar range gate is fully represented by its second-order Fourier expansion in β as

$$V_r = A_0 + A_1\cos\beta + B_1\sin\beta + A_2\cos2\beta + B_2\sin2\beta, \tag{15}$$

in which

$$A_0 = r\cos^2\phi[(\partial u/\partial x) + (\partial v/\partial y)] + 2(w + V_f)\sin\phi, \tag{16}$$

$$A_0 = -v_0\cos\phi, \tag{17}$$

$$B_1 = -u_0\cos\phi, \tag{18}$$

$$A_2 = r\cos^2\phi[(\partial u/\partial x) - (\partial v/\partial y)]/2, \tag{19}$$

$$B_2 = -r\cos^2\phi[(\partial v/\partial y) + (\partial u/\partial x)]/2. \tag{20}$$

The Fourier coefficients A_0–B_2 can either be directly calculated along the circle (r, ϕ) described in azimuth by the range gate (Browning and Wexler 1968), or obtained by a least squares fitting process between measured and calculated radial winds V_r (Bréger 1977). In that case the following expression

$$P = \sum_N (V_{r\,\text{measured}} - A_0 - A_1\cos\beta - B_1\sin\beta - A_2\cos2\beta - B_2\sin2\beta)^2 \tag{21}$$

is minimized with respect to the five unknowns of A_0–B_2. The least squares approach was used in the present case because it does not need regular data filling along the circle, as does the direct Fourier approach.

Finally, the analysis of V_r in azimuth along each circle (r, Φ) directly yields u_0, v_0, $[(\partial u/\partial x) - (\partial v/\partial y)]$, and $[(\partial u/\partial y) + (\partial v/\partial x)]$ at the scale of the analyzed circle.

As for the divergence $[(\partial v/\partial y) + (\partial u/\partial x)]$ and V_F, there are two possible cases:

1) If $w \ll V_F$, which corresponds to stratiform situations, then they are obtained separately by analyzing in an altitude slab that is 200 m thick, with the coefficient A_0 obtained in the various gates i at elevations j incoming in the slab. Then, writing $A_0/\sin\phi j = r_i^2 \cos^2\phi j/z_0[(\partial v/\partial y) + (\partial u/\partial x)] + V_F$, a simple linear regression on the couple $A_0/\sin\phi j$, $r_i^2 \cos^2\phi j)$, allows for the retrieval of the divergence and V_F. The obtained divergence and V_F are mean values at the mean scale of the analyzed gates. Gathering u_0, v_0, and the deformations into the same altitude slabs also allows average values of these parameters to be obtained. Finally, w is obtained by integrating the horizontal divergence with altitude.
2) If w is of the order of V_F, then the process described previously in 1 allows $(W + V_F)$ and $[(\partial v/\partial y) + (\partial u/\partial x)]$ to be obtained. Then, w is obtained by integrating $[(\partial v/\partial y) + (\partial u/\partial x)]$ at low elevation and subtracting it from $(w + V_F)$ in order to calculate V_F. This corresponds to moderately convective areas.

2) Analysis of radar reflectivity η and Q_{TOT} derivatives

In a way, similar to the wind, it is easy to calculate the reflectivity η and its horizontal derivatives by adapting the VAD analysis to reflectivity (or RAD). Both η and η_0 are reflectivities at points M and M_0, respectively (Fig. 1).

Let η be linear as a function of x and y

$$\eta = \eta_0 + x\,\partial\eta/\partial x + y\,\partial\eta/\partial y. \tag{22}$$

We may write

$$\eta = \eta_0 + \partial\eta/\partial x(r\cos\phi\cos\beta) + \partial\eta/\partial y(r\cos\phi\sin\beta). \tag{23}$$

A number of measurements N are gathered along the circle with radius $r\cos\phi$ described by point M about M_0. The unknowns η_0, $\partial\eta/\partial x$, and $\partial\eta/\partial y$, which are the mean values of the reflectivity and its horizontal derivatives along the circle, are retrieved by minimizing in the least squares sense, which is the expression P derived from Eq. (11) with respect to them for all experimental points along the circle,

$$P = \sum_N [\zeta_{\mathrm{measured}} - \eta_0 - \partial\eta/\partial x(r\cos\phi\cos\beta) - \partial\eta/\partial y(r\cos\phi\sin\beta)]^2. \tag{24}$$

Thus,

$$N\eta_0 - r\cos\phi\sum_N \sin\beta\,\partial\eta/\partial x - r\cos\phi\sum_N \cos\beta\,\partial\eta/\partial y = \sum_N \zeta_{\mathrm{measured}}, \tag{25}$$

$$\eta_0\sum_N \sin\beta - r\cos\phi\sum_N \sin^2\beta\,\partial\eta/\partial x - r\cos\phi \times \sum_N \sin\beta\cos\beta\,\partial\eta/\partial y = \sum_N \zeta_{\mathrm{measured}}\sin\beta, \tag{26}$$

$$\eta_0\sum_N \cos\beta - r\cos\phi\sum_N \sin\beta\cos\beta\,\partial\eta/\partial x \times \sum_N -r\cos\phi\sum \cos^2\beta\,\partial\eta/\partial y = \sum_N \zeta_{\mathrm{measuerd}}\cos\beta. \tag{27}$$

Solving the previous linear system of equations provides the unknowns η_0, $\partial\eta/\partial x$, and $\partial\eta/\partial y$.

Because Eq. (23) is also a Fourier expansion at the first order with respect to azimuth β, the unknowns can also be directly derived as Fourier coefficients. However, if both methods are mathematically equivalent, the direct Fourier calculation needs a regular measurement repartition, while the least squares calculations suffers irregular or incomplete filling.

Thus, η_0, $\partial\eta/\partial x$, and $\partial\eta/\partial y$ are derived along each circle at the radar vertical. Then, $\partial\eta/\partial z$ is directly deduced from η at two consecutive altitudes. The time derivative $\partial\eta/\partial t$ is deduced from consecutive sequences chosen as immediately before and after the current "central" sequence on which the space derivatives $\partial\eta/\partial x$, $\partial\eta/\partial y$, and $\partial\eta/\partial z$ are computed. Calculations show that $\partial q_p/\partial x$, $\partial q_p/\partial y$, and $\partial q_p/\partial t$ are not too sensitive to noise measurements and thus do not fluctuate with altitude, while $\partial q_p/\partial z$ does. Thus, in order to improve accuracy on $\partial q_p/\partial z$, the $q_p(z)$ profile was regularized by linear fitting over three points.

d. Temporal and spatial scales

The temporal derivative is calculated on a time covering three sequences, and thus it is representative of an about 20–30-min scale while the space derivatives that are calculated during the central sequence over various selected radar ranges are representative of scales of these ranges (typically 20–100 km) within a sequence of 8-min duration.

Vertical derivatives are calculated over altitude slices of 200 m, which is the corresponding vertical characteristic scale.

Because all calculations are performed under the hypothesis that the wind and the reflectivity vary linearly on the horizontal, then only the resolved tendencies are analyzed. Smaller-scale motions and organizations of reflectivity, including wave-like and turbulence structures, can be obtained by subtracting the observed radial wind or reflectivity from the first-order (constant + linear) signal obtained by means of the previously described method.

Note that in this case these smaller-scale motions have a mean value that is close to zero because they correspond to the residual of the least squares fitting process.

e. Uncertainties and errors

Several causes induce errors in the calculation of dq_p/dt, and ultimately the Q_2 estimation.

As shown by Eq. (10), which provides the relationship between radar-deduced parameters and dq_p/dt, errors on radar reflectivity, wind, and their derivatives induce errors on dq_p/dt. In the following subsection, we consider whether these are the errors directly resulting from the method and its implementation. However, physical causes can also provide errors or biases that are considered in sections 2e(2) and 2e(3).

1) PRECISION ON THE RETRIEVED PARAMETERS, WHICH IN TURN INDUCES ERRORS ON Q_2

Errors on Q_2 mainly result from uncertainties about winds (and their derivatives), the terminal fall velocity, and the reflectivity (and its derivatives) and its relationship with the water content.

These various uncertainties are considered below.

(i) Errors on u, v, w, and V_F

Equations (16)–(20) show that errors on wind components and their derivatives are related to errors on the Fourier coefficients A_0, A_1, B_1, A_2, and B_2. Errors on Fourier coefficients are in turn related to errors on the radar radial wind δV_r.

For example, because $A_1 \approx \Sigma_N V_r \cos\beta$, then $\delta A_1 = \delta V_r / N^{0.5}$, which results in $\delta A_1 = \pm 0.025$ m s^{-1} for $N = 400$ and $\delta V_r = 0.5$ m s^{-1}. Thus, because $A_1 = -v_0 \cos\Phi$, $\delta v_0 = \pm 0.025$ m s^{-1}. Similarly, $\delta u_0 = \delta v_0 = \pm 0.025$ m s^{-1}, and $\delta W = \pm 0\,23$ cm s^{-1} = 0.0023 m s^{-1} and $\delta V_F = \pm 0.06$ m s^{-1} from measurements at high elevation.

(ii) Errors on reflectivity η and q_p

Errors on the reflectivity and its space derivatives obtained by the RAD analysis are related to the errors on the Fourier coefficients, which in turn are related to the error on the measured radar reflectivity [see Eqs. (25)–(27)].

The error on the reflectivity factor is estimated as ± 0.056 dBZ, which results in a reflectivity error $\delta\eta/\eta = \pm 1.3\%$ (η is multiplied by a factor of between 1.013 and 0.987). Thus, $\delta q_p/q_p = b\delta\eta/\eta \approx 0.08\%$.

(iii) Errors on η and q_p derivatives

Maximal errors on η derivatives are estimated as

$$\delta(\partial\eta/\partial x)/\partial\eta/\partial x = \delta(\partial\eta/\partial y)/\partial\eta/\partial y \approx 9\%,$$

$$\delta(\partial\eta/\partial z)/\partial\eta/\partial z = 1.3\%; \quad \delta(\partial\eta/\partial t)/\partial\eta/\partial t \approx 1.9\%.$$

Now, because

$$\partial q_p/\partial x = (bq_p/\eta)\partial\eta/\partial x; \quad \text{then} \quad \delta(\partial q_p/\partial x)/\partial q_p/\partial x = \delta q_p/q_p + \delta\eta/\eta + \delta(\partial\eta/\partial x)/\partial\eta/\partial x \approx 10.4\%.$$

Similarly,

$$\delta(\partial q_p/\partial y)/\partial q_p/\partial y \approx 10.4\%;$$

$$\delta(\partial q_p/\partial z)/\partial q_p/\partial z \approx 3.4\%;$$

$$\delta(\partial q_p/\partial t)/\partial q_p/\partial t \approx 1.9\%.$$

Estimation of the total error on dq_p/dt is provided by considering Eq. (10) in which the errors on $\partial q_p/\partial x$ and $\partial q_p/\partial y$ are important but $\partial q_p/\partial x$ and $\partial q_p/\partial y$ themselves are small, the error on $\partial q_p/\partial t$ is small while the term $\partial q_p/\partial t$ is medium, and, finally, the error on $\partial q_p/\partial z$ is small but $\partial q_p/\partial z$ is stronger.

Finally, the total relative error on dq_p/dt, and thus on Q_2, can be estimated as $\approx$32%.

This error does not take into account possible systematic errors resulting from physical causes and biases as examined in the next subsections.

2) PHYSICAL UNCERTAINTIES

As seen in section 2b(1), some weak signals may be lost. Thus, it can be estimated that q_p is underestimated by about 5%.

Reflectivity and mixing ratio are related by empirical formulas $q_{\text{tot}} = A\eta^b$, where A and b depend on the hydrometeor type. In particular ice hydrometeors cannot be precisely determined, and their characteristics may vary significantly. However, some elements of checking exist, for example, the terminal fall velocity V_F calculated by the method, allows for discrimination between graupel (2–3 m s^{-1}) and snow (0.5–1 m s^{-1}). Another type of checking is provided by Evaristo et al. (2010), who use an

algorithm of hydrometeor classification on the same dataset as the present study, and also identify the presence of graupel among other types of ice hydrometeors. Checking using V_F and hydrometeor identification was done in parallel to the present study. Both the A and b parameters were taken from Hauser and Amayenc (1986) in their study of a tropical squall line observed in the northern Ivory Coast in June 1981 during COPT 81. Namely, in the rain phase, $A = 1.73 \times 10^{-6}$; $b = 0.613$; in the ice phase, we took the parameters from snow in a convective region, that is, $A = 8.0 \times 10^{-6}$; $b = 0.605$ (Marécal 1992). This choice can become sensitive, particularly in ice, to some mixing with other hydrometeors or by considering stratiform regions. In the case of graupel in a more stratiform situation, $A = 2.72$ and $b = 0.571$. Note that q_{tot} and Q_2 are proportional to the parameter A. Thus, a modification on A directly impacts these parameters but does not change their vertical tendency or their signs. Parameter b has a typical variation range of 0.5–0.7. When $b = 0.6 \pm 0.1$, variations by ± 0.1 impact q_{tot} and Q_2 moderately for low reflectivities ($\pm 50\%$ at 20 dBZ), and strongly for reflectivities of 50 dBZ (by a factor of 3).

3) Bias resulting from the range dependence of measurements

When the range increases above a certain threshold, say 20 km, partial beam filling and convolution of reflectivity signals can induce a negative bias in reflectivity. For example, Chumchean et al. (2004) have shown that a simple scaling paradigm was applicable in order to correct long-distance reflectivities with respect to 20-km measurements taken as a reference, and ensure uniformity distributions of reflectivity between the near- and far-range measurements. This effect depends on the 3-dB beamwidth and increases with it. It also increases with the observation range. The RONSARD 3-dB beamwidth is only 0.9° and the maximal range is 30 km; thus, the bias on reflectivity is weak: it would be in the worst case (at 30 km) 1.2 dB for a 30-dBZ cell, and 2 dB for a 50-dBZ cell. Because data are processed over a distance of 0–30 km, and because up to 20 km the effect is weak, it is reasonable to retain 0.6 dB for 30-dBZ cells and 1 dB for 50-dBZ cells. The total reflectivity bias is thus weak.

The effect on wind is even weaker because only the maximum of the Doppler spectrum is taken into account, while for the reflectivity one must consider the spectrum area.

f. Q_2 units and normalization

In section 3, Q_2 is expressed in kelvins per second. As explained in section 4, for comparison with other studies, Q_2 will be normalized by the effective rain rate during the time of Q_2 evaluation.

3. Example of Q_2 estimates within three squall lines

During the AMMA SOP, 43 convective systems or isolated convective episodes were observed in north Benin. In the present work, estimates of Q_2 (using the analysis described in section 2) are performed within three squall lines that are characterized by a well-defined structure that is more or less two-dimensional, observed on 28 July, 30 June, and 12 September 2006. These three squall lines are described when they are within the RONSARD radar range, that is, at 100- or 200-km radius, depending on the observation mode. These cases were selected because each of them corresponds to a given phase in the evolution of the West African monsoon, namely, pre-onset for 30 June, onset for 28 July, and the beginning of decay for 12 September.

The analysis is done retaining all of the data in the 30-km range about the radar in order to focus on the convective and stratiform components of the moisture budget. The processing was also performed at 100-km horizontal scale and evidenced minor differences with the 30-km scale processing, except within convective areas that are filtered out at this 100-km scale. In the following, only 30-km scale processing is shown and discussed.

The analysis is applied to the three selected squall lines as follows:

- from 0743 to 0933 UTC 30 June 2006, that is, 14 sequences (each sequence providing a Q_2 profile);
- from 0422 to 0756 UTC 28 July 2006, that is, 28 profiles; and
- from 1614 to 1857 UTC 12 September 2006, that is, 20 profiles.

Within stratiform precipitation, the vertical velocity profile w with respect to altitude z is generally observed to be negative (subsiding) below the 0°C isotherm, and positive above. The purely positive (negative) profile of w along the troposphere is indicative of convective development (decay).

a. Results for the 28 July squall line

The 28 July squall line was within the RONSARD radar range between 0416 and 1000 UTC. The reflectivity factor Z on horizontal cross sections at 1500-m altitude from 0601 to 0726 UTC (Fig. 2) evidences a convective line that is oriented northwest–southeast in the north of the system, and a second branch that is oriented southwest–northeast in its southern part. This

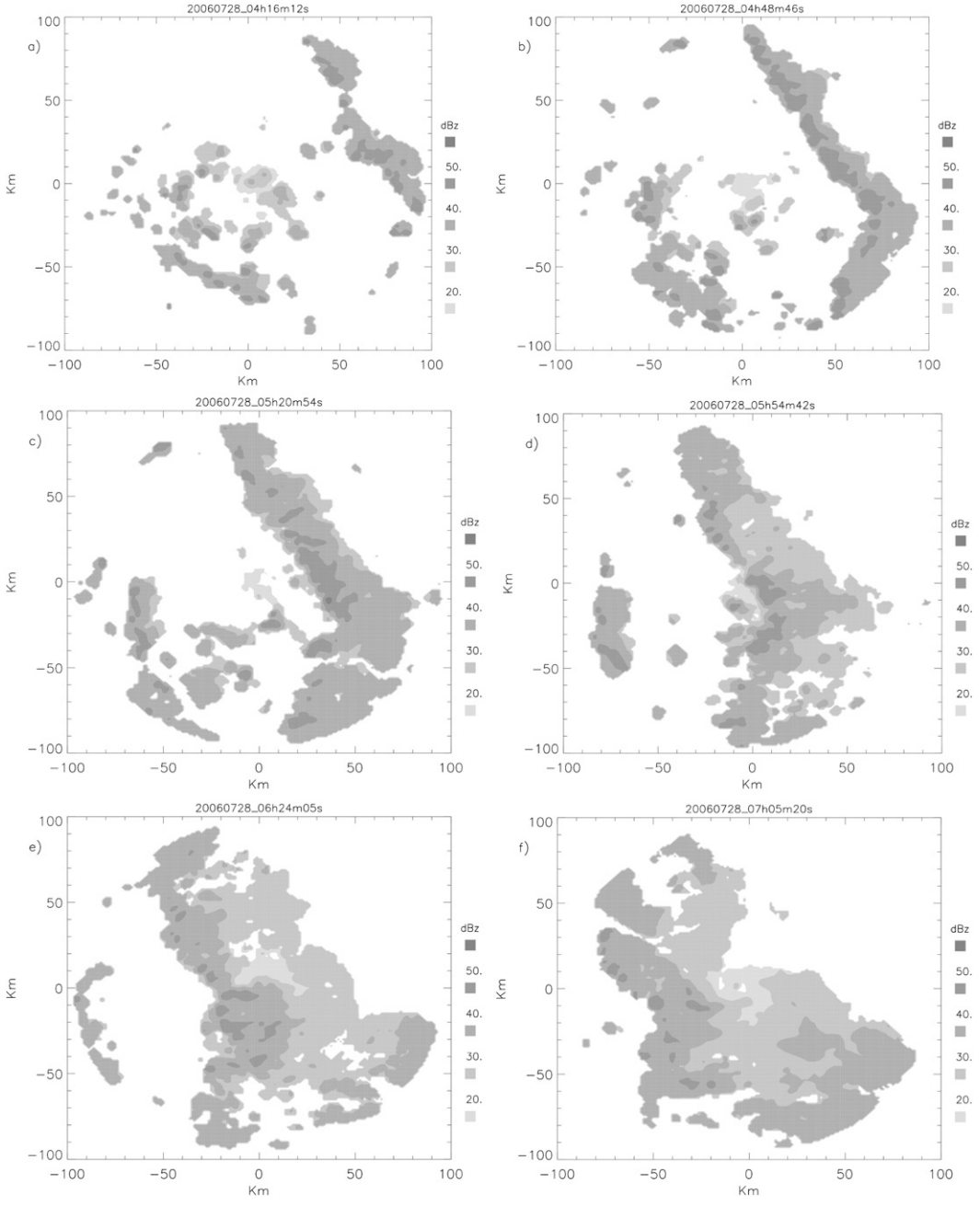

FIG. 2. Time evolution of horizontal radar reflectivity at (a) 0416, (b) 0448, (c) 0520, (d) 0554, (e) 0624, and (f) 0705 UTC 28 Jul 2006.

double line crosses over the radar area to the southwest and progressively evolves to a patchy pattern, with a stratiform part toward the rear.

Figures 3–6 display the time evolution of vertical profiles of the reflectivity (Fig. 3), the terminal fall velocity (Fig. 4), and the horizontal (Fig. 5) and vertical (Fig. 6) components of the wind, respectively, as deduced from the VAD analysis.

At 0601 UTC the VAD analysis is performed in an area encircling one element of the convective part of the squall line. In this area below 5-km altitude (Fig. 5a) the leading part of the typical cold outflow from squall lines is observed, showing southwestward winds with a maximum value of 10 m s^{-1} at 1.5-km altitude. Later on, this flow strengthens to reach maximum values of 14 m s^{-1} at 3-km altitude at 0630 UTC (Fig. 5b), 17 m s^{-1} at

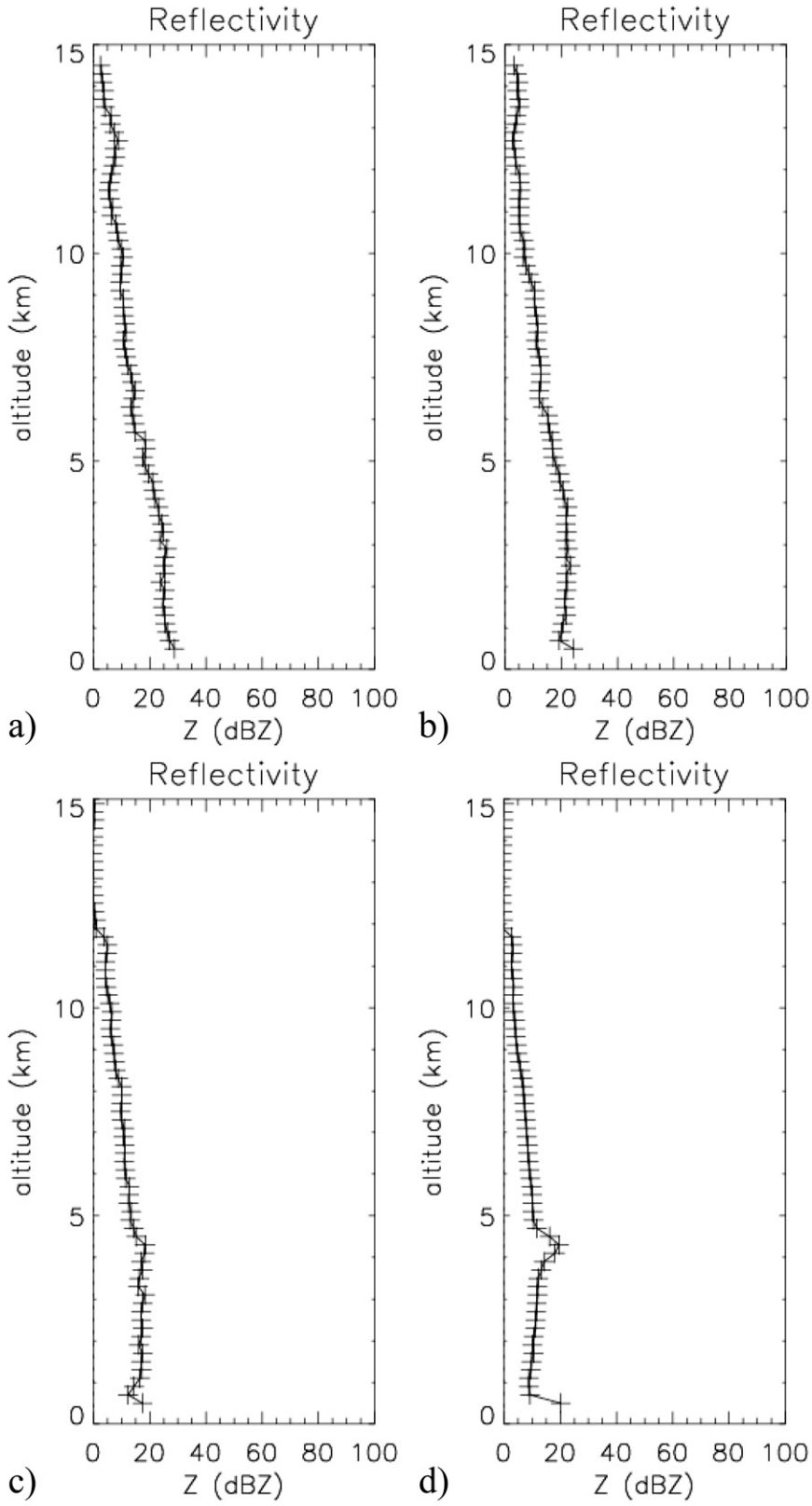

FIG. 3. Reflectivity profile (dBZ) at (a) 0601, (b) 0630, (c) 0651, and (d) 0726 UTC.

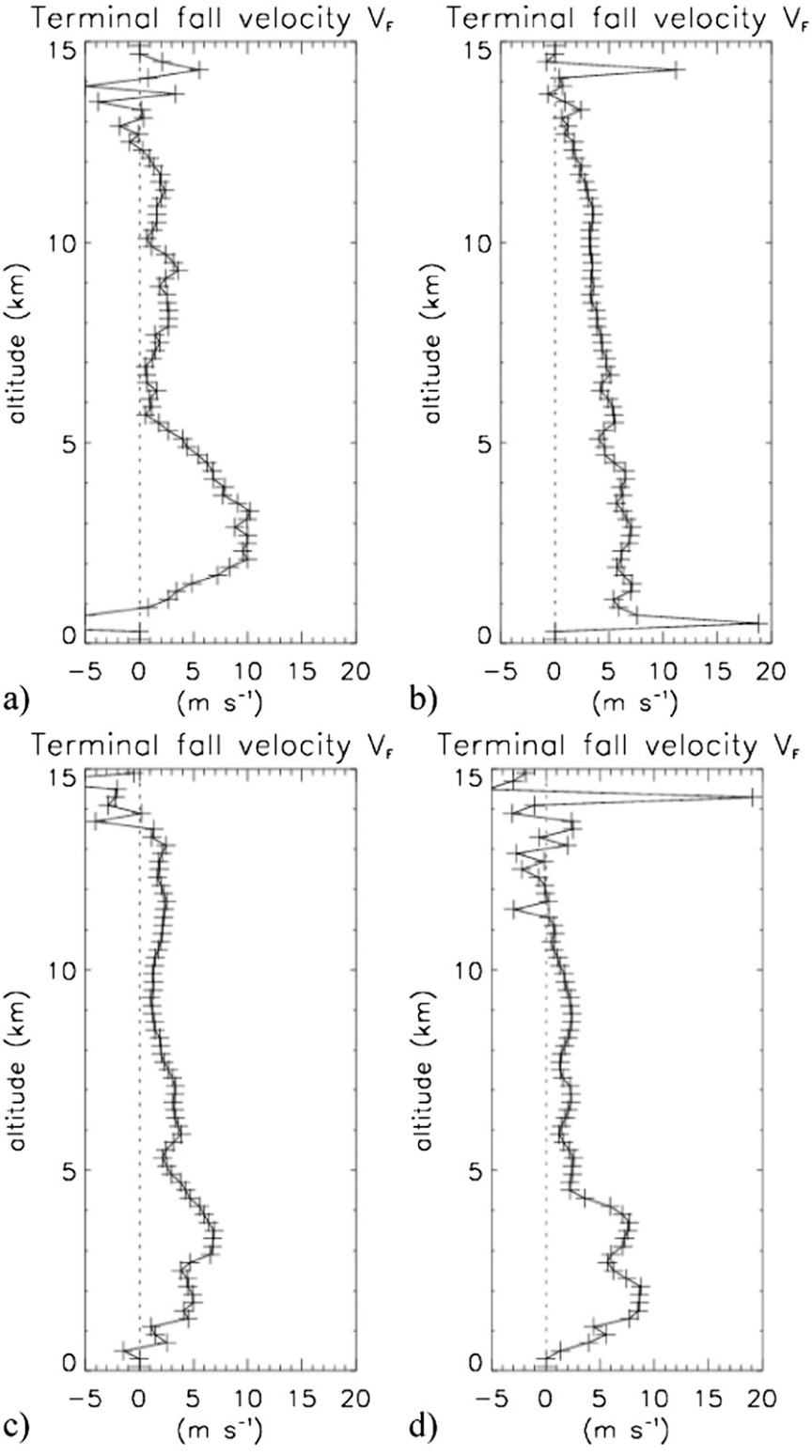

FIG. 4. Terminal fall velocity profile (m s^{-1}) at (a) 0601, (b) 0630, (c) 0651, and (d) 0726 UTC.

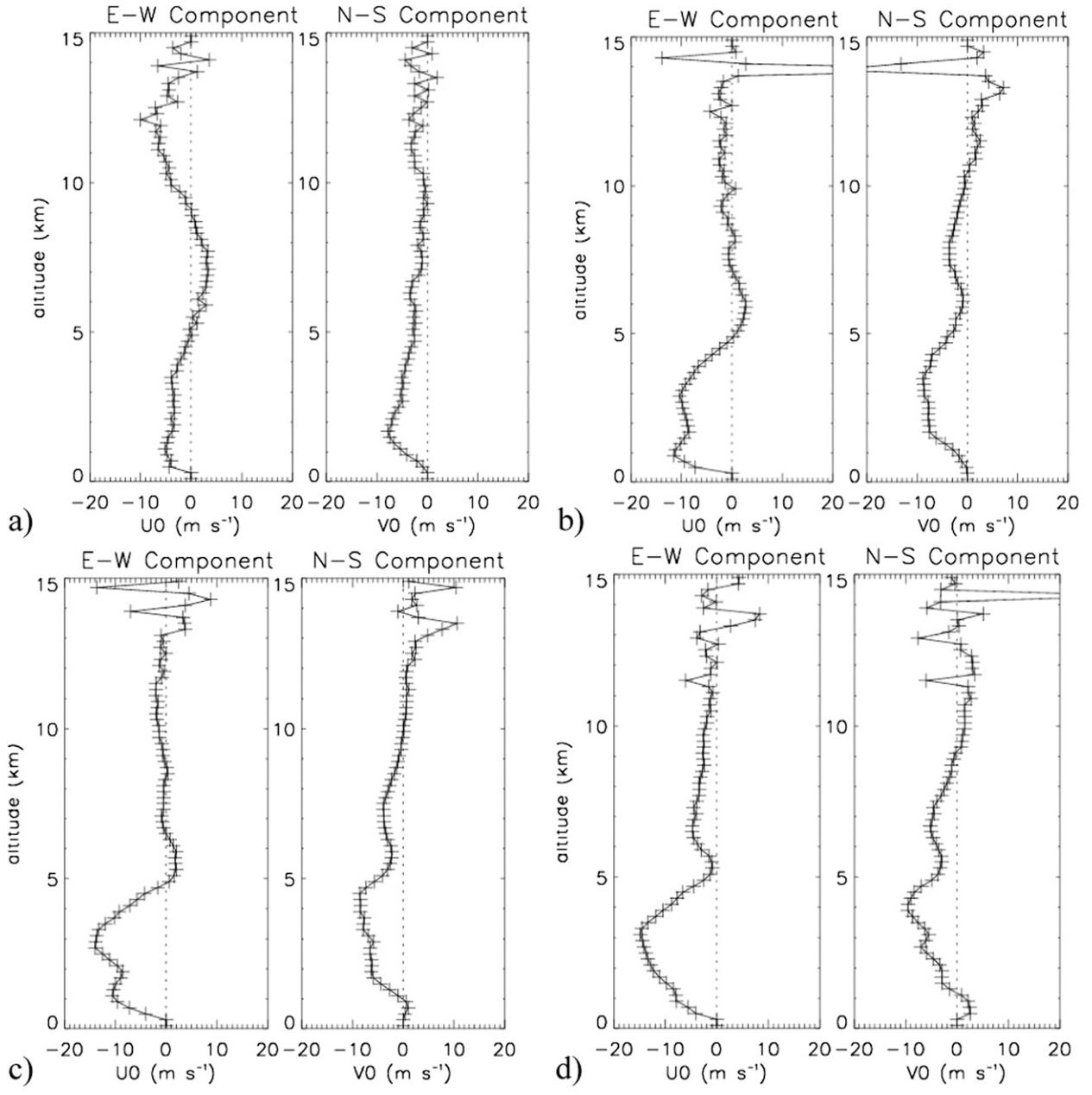

FIG. 5. Horizontal wind components profiles (left) u_0 and (right) v_0 (m s^{-1}) at (a) 0601, (b) 0630, (c) 0651, and (d) 0726 UTC.

3.5 km and 0651 UTC (Fig. 5c), and 19 m s^{-1} at 4 km and 0726 UTC (Fig. 5d), indicating a tilt of the layer with the rear-to-front flow. The vertical profile of reflectivity evolved from a linearly decreasing profile to a profile typical of stratiform precipitation with a well-defined bright band indicating a 0°C isotherm around 4.5-km altitude (see Figs. 3a–d). The vertical velocity indicates the presence of ascending motion throughout the troposphere in the convective region with a maximum located at 3–4-km altitude in the front part (0601 UTC, Fig. 6a) and at 8 km rearward (0630 UTC, Fig. 6b). The transition zone (0651 UTC, Fig. 6c) is characterized by subsiding motion, and the stratiform area is characterized by downdrafts below 6 km and mesoscale updrafts above (Fig. 6d). The associated vertical profile of terminal fall velocity shows the presence of relatively high values up to 10 m s^{-1} for the liquid phase and 2.5 for the ice phase (Figs. 4a–d). In the transition zone, V_F appears smaller (see, e.g., 0630 UTC, Fig. 4b). Below 1.5-km altitude and in the convective region a negative correlation between the terminal fall velocity and the reflectivity is observed. While the terminal fall velocity

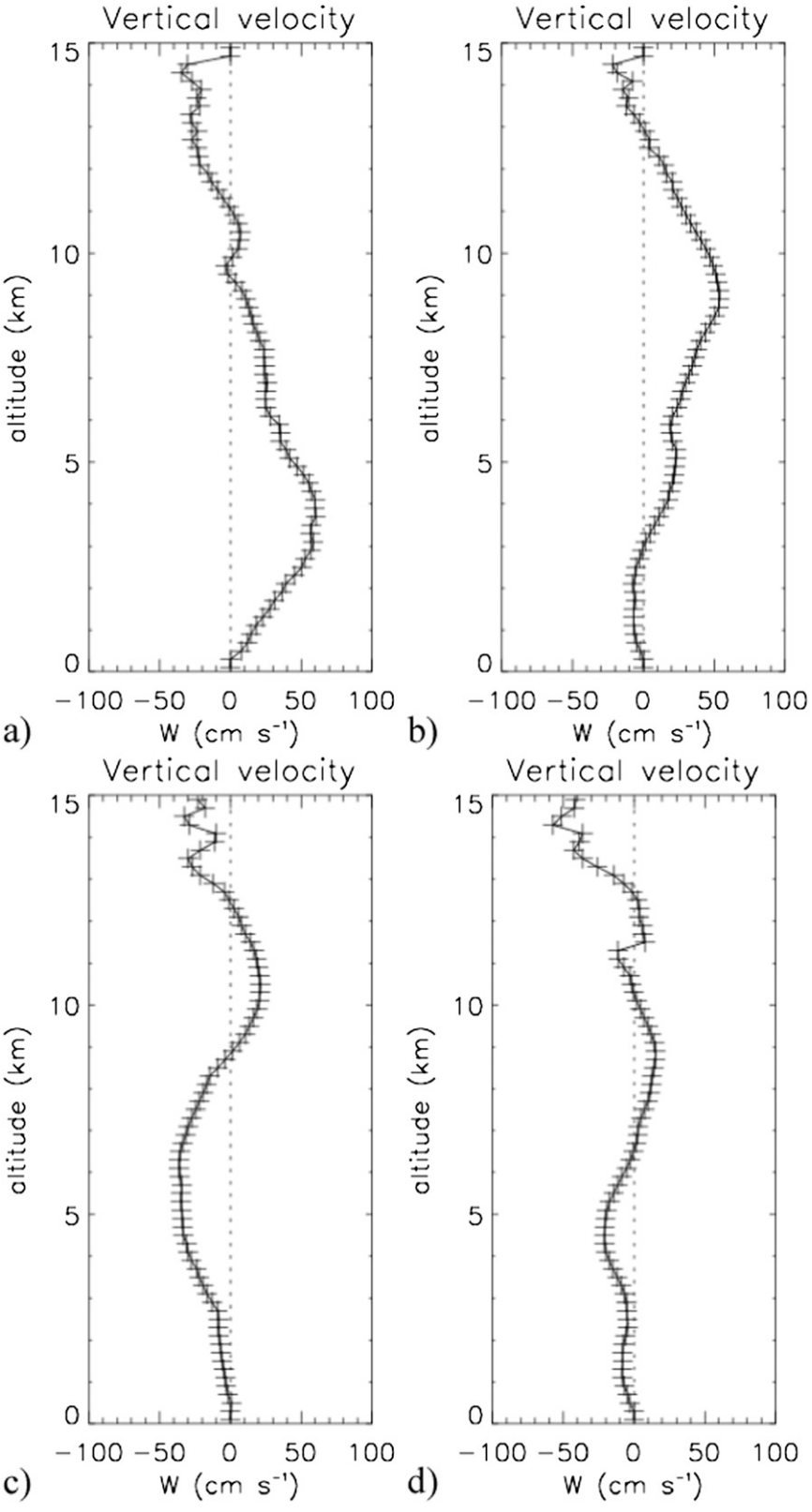

FIG. 6. Vertical velocity profile (cm s^{-1}) at (a) 0601, (b) 0630, (c) 0651, and (d) 0726 UTC.

decreases the reflectivity increases or remains quasi constant. The slope change in the V_F profile appears to be located at the altitude where Evaristo et al. (2010) observed a transition between graupel and moderate rain by using a hydrometeor classification algorithm applied to RONSARD data.

In the convective region (Fig. 7a) in which the vertical velocity W is positive, the Q_2 profile exhibits a convective structure with moisture loss ($Q_2 > 0$) throughout much of the troposphere. The Q_2 profiles derived from the VAD–RAD analysis show remarkably similar tendencies in the transition and stratiform regions (Figs. 7b–d). They are characterized by a moisture source ($Q_2 < 0$) below 3–4 km, primarily resulting from rainfall evaporation, a moisture sink ($Q_2 > 0$) above and up to 7–10 km, and a generally small moisture sink (and less frequently moisture production) above 10 km. The maximal Q_2 production is from about -1 to -3 K s^{-1}. The moisture Q_2 loss ranges between $+1$ and $+6$ K s^{-1}. These profiles exhibit a great variability, and after averaging them, the mean moisture production and loss are evaluated to be about -1×10^{-3} K s^{-1} and $+2 \times 10^{-3}$ K s^{-1} respectively. The moisture production at low levels could be due to evaporation, which releases moisture from clouds to their environment, while the moisture loss above could be due to condensation (or to ice deposition), which produces clouds at the expense of their environment.

In the transition region (Fig. 7b) the profile exhibits a mixed stratiform–convective structure with moisture loss ($Q_2 > 0$) below 2 km through the removal of water vapor by net condensation and slight drying between 1.5 and 3 km (convective characteristic), and moisture loss above, with two peaks at 4 and 5.5 km.

The double-peak structure results from the combined effect of vertically separated peaks in drying from the convective part (near 4 km) and the stratiform part (near 6 km). As explained by Johnson (1984), these peaks occur at the levels of maximum removal of water vapor by net condensation.

b. Results for the 30 June squall line

Figure 8 show the 30 June squall-line evolution from 0622 to 0913 UTC. Within the radar range, this squall line also shows up as a convective line oriented northwest–southeast. It is composed of two elements that are oriented slightly more to the west between 0630 and 0700 UTC (Figs. 8a,b). The line is moving to the west-southwest until 0805 UTC (Figs. 4c,d). While this main line moves more slowly about 0840 UTC, weaker cells develop to the east. From 0913 to 0955 UTC, the main line is oriented north–south, and other strong but smaller cells develop in the eastern part of the domain (Figs. 8e,f). Between these two cells, a large zone of weaker rain (reflectivity) covers

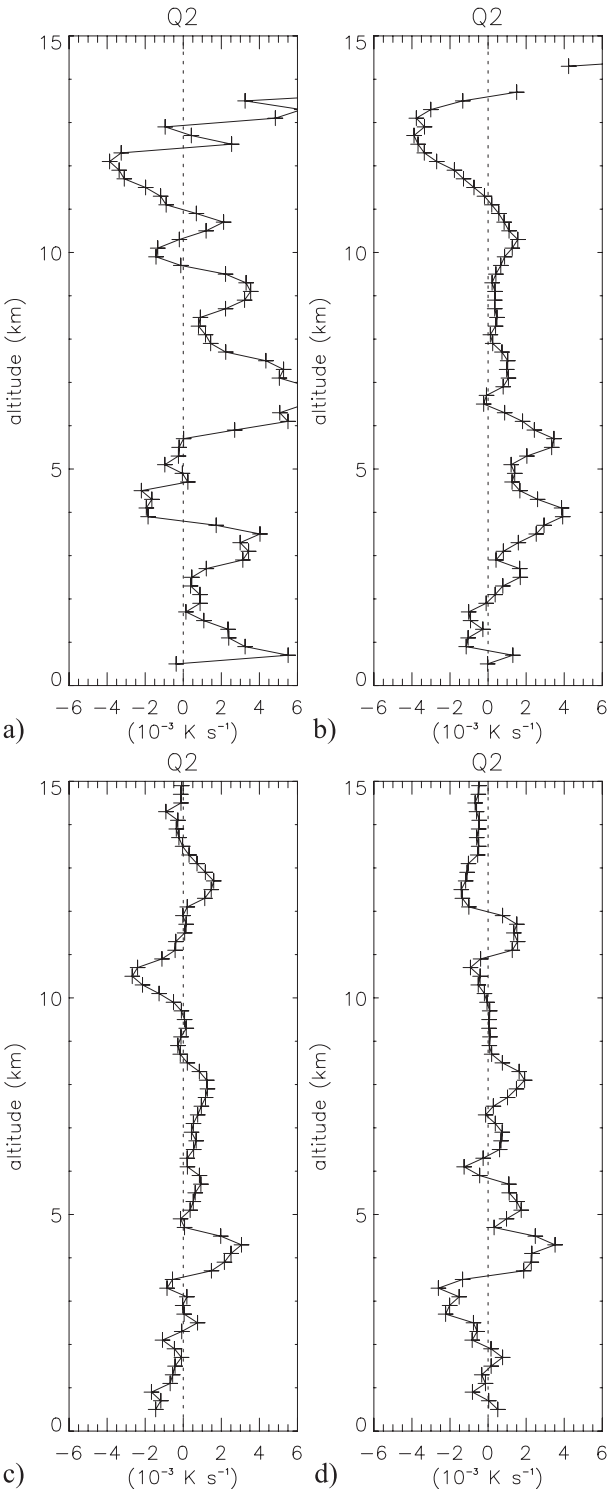

FIG. 7. The Q_2 profile (abscissa, 10^{-3} K s^{-1}) as a function of altitude (ordinate, km) at (a) 0554, (b) 0630, (c) 0651, and (d) 0705 UTC 28 Jul 2006.

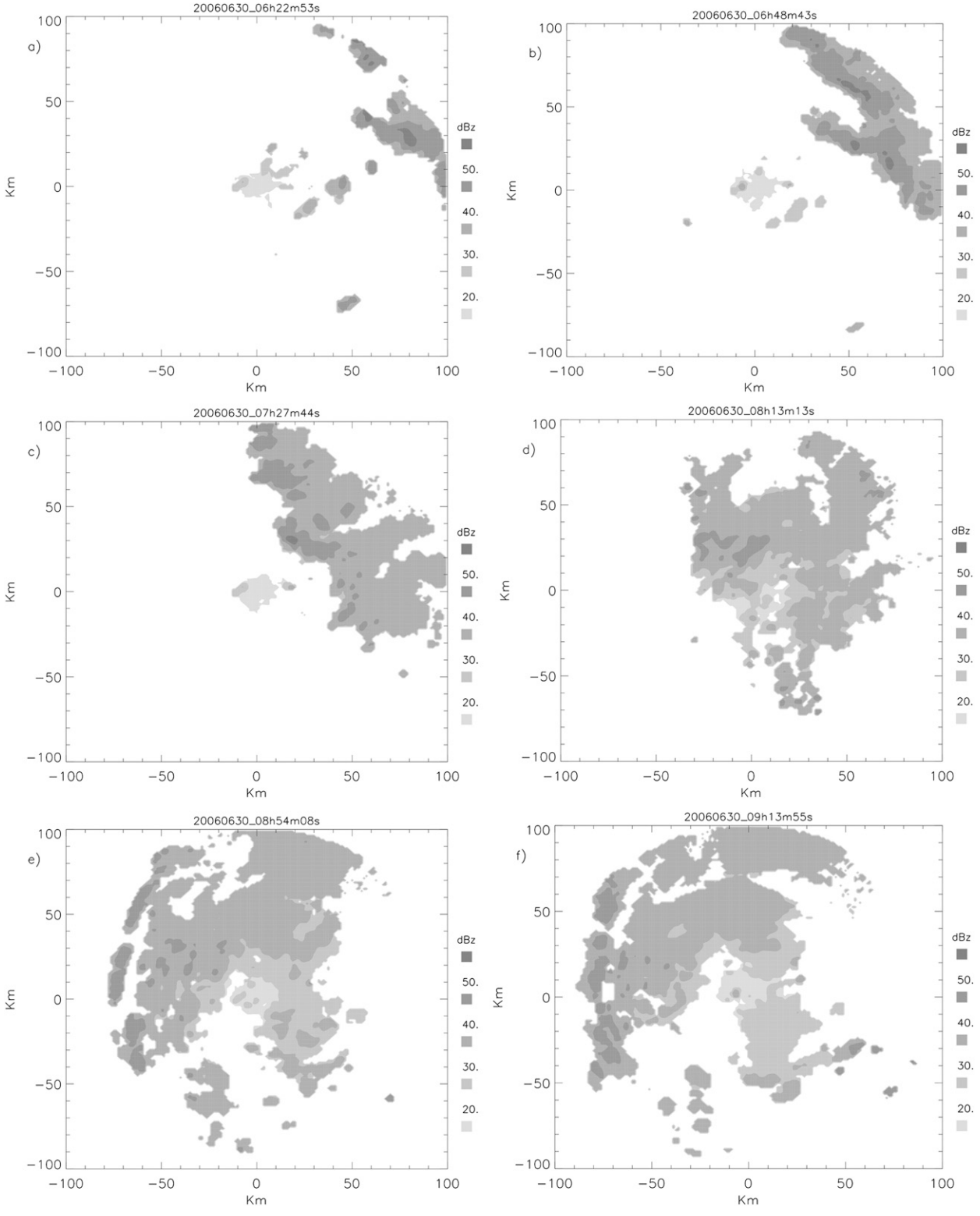

FIG. 8. Time evolution of horizontal radar reflectivity at (a) 0622, (b) 0648, (c) 0727, (d) 0813, (e) 0854, and (f) 0913 UTC 30 Jun 2006.

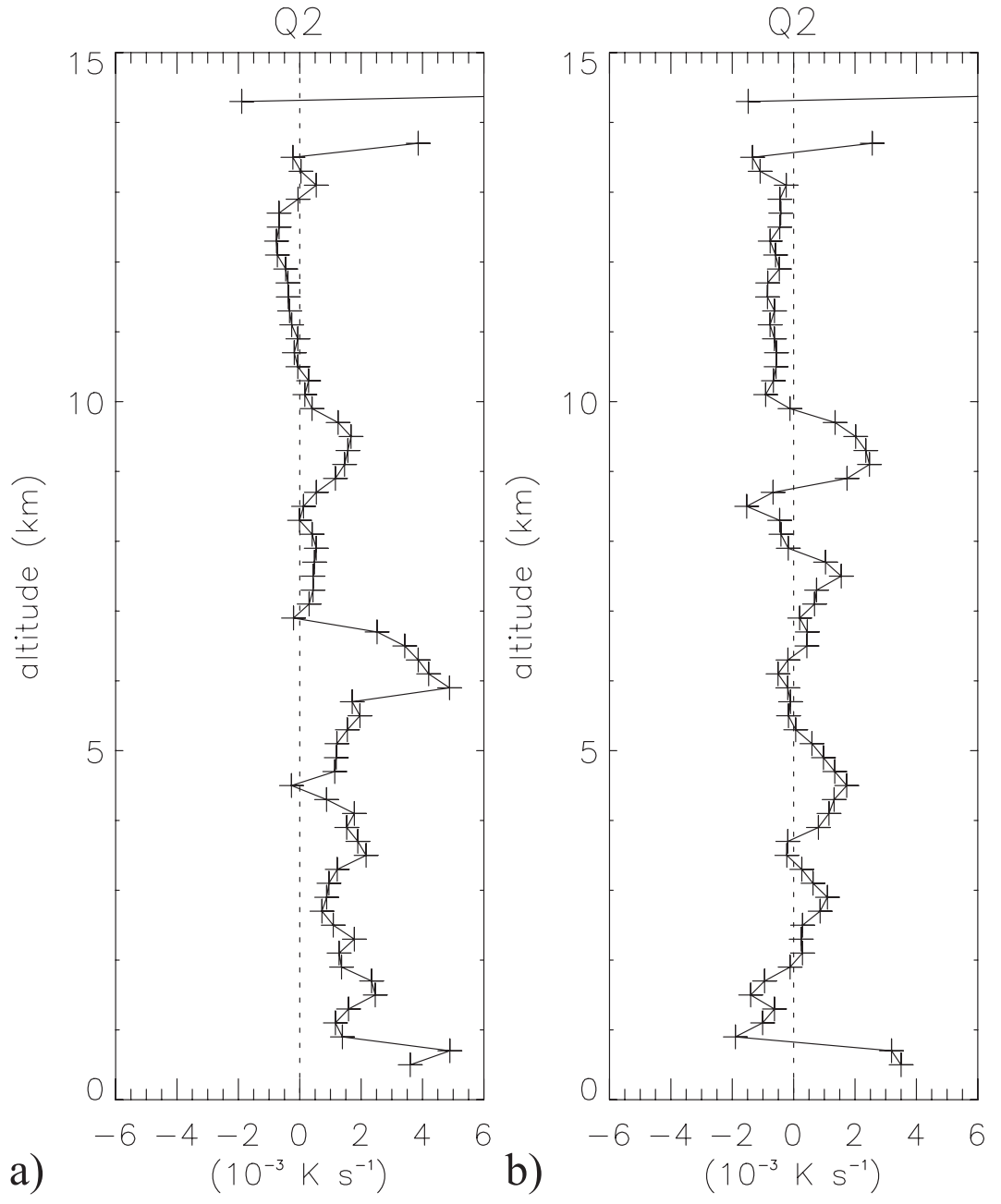

FIG. 9. The Q_2 profile (abscissa, 10^{-3} K s^{-1}) as a function of altitude (ordinate, km) at (a) 0813 and (b) 0837 UTC 30 Jun 2006.

about 100-km width. At 1014 UTC, the eastern cell is the only one remaining in the radar range (not shown). This is also illustrated by the evolution of the rain rate (deduced from disdrometer measurements; N. Viltard 2008, personal communication) from 0743 to 0927 UTC, namely, 6.95 mm h^{-1} at 0743 UTC, 6.25 mm h^{-1} at 0805 UTC, 6.09 mm h^{-1} at 0813 and 0819 UTC, 7.42 mm h^{-1} at 0854 UTC, 6.72 mm h^{-1} at 0900 UTC, 7.19 mm h^{-1} at 0907 UTC, 7.42 mm h^{-1} at 0914 UTC, 8.9 mm h^{-1} at 0920 UTC, and 9.84 mm h^{-1} at 0927 UTC. Rain-rate starts to decrease during the passage of the first cell, stays at a lower value corresponding to stratiform precipitation, and increases again when the second convective cell moves into the radar range.

From 0743 to 0933 UTC Q_2 is calculated. The Q_2 profiles exhibit moisture loss from 0743 to 0819 UTC throughout

the troposphere (e.g., at 0813 UTC, see Fig. 9a). As in the case of 28 July, moisture loss appears well correlated with $w > 0$. From 0826 UTC, the Q_2 profile takes a mixed stratiform/convective structure, with $Q_2 < 0$ between 1 and 2 km, and $Q_2 > 0$ above (e.g., at 0837, see Fig. 9b). The mean moisture loss is about $+2\ 10^{-3}$ K s^{-1}.

c. Results for the 12 September squall line

Figure 10 shows the squall line within the radar range between 1500 and 1900 UTC. At 1500 UTC (not shown) the system is weak, and then from 1600 UTC it reinforces and shows up as a structure that is aligned north–south and moves to the west (Figs. 10a,b). Around 1700 UTC, it comes over the radar (Figs. 10c,d). Then after 1800 UTC (Figs. 11e,f), the system exhibits a classical pattern composed of a convective part toward the west, followed by a reflectivity minimum and an extensive stratiform part to the rear (to the East). After 1900 UTC, the structure dissipates (not shown).

The Q_2 profile is calculated from 1614 to 1857 UTC. The Q_2 profiles from 1614 to 1733 UTC oscillate between two structures (e.g., 1720 and 1733 UTC, see Figs. 11a,b): the first one is positive throughout the troposphere, exhibiting a convective character, the second is negative below 1.5–3 km, positive above, more characteristic of a mixed convective–stratiform structure. The moisture loss ranges between $+2$ and $+5\ 10^{-3}$ K s^{-1}, and the mean moisture loss is about $+2.5\ 10^{-3}$ K s^{-1}.

4. Discussion

The present results are evidence of the systematic behavior of the Q_2 profile found for the three selected cases characterizing the various phases of the monsoon cycle. They show, in particular, two typical structures, with either moistening below 3–4 km and drying above, with a peak around 5 km; or a double peak of drying at 1 km and 4–5 km, with moistening between and above. For each of these typical profiles a relative variability with height is observed.

The Q_2 profiles also exhibit great variability from case to case, so that averaging must be done before evaluating these results against other estimates. For the three cases presented here, the mean Q_2 loss (production) was estimated as $+2.2\ 10^{-3}$ K s^{-1} ($-1\ 10^{-3}$ K s^{-1}). On the other hand, as shown in most studies, Q_2 (and also Q_1 values) must be normalized to the mean rain rates (RRs) during the time of measurement (or simulation) so that temperature and moisture budgets are consistent. In the present cases, the rain rates were measured by two rain recorder instruments located close to and 22 km southeast of RONSARD radar. Thus, the normalized moisture loss Q_{2N} is defined as Q_2/RR (K cm^{-1}) if Q_2 and RR are measured during the same time (about 2–3 h for the present cases). Thus, on an hourly basis, the mean rain rates for the three studied days are 0.729, 0.577, and 0.5 cm h^{-1}, for 30 June, 28 July, and 12 September, respectively, that is, a mean rain rate 0.61 cm h^{-1}.

This way, the mean normalized moisture loss (production) Q_{2N} can be estimated as $Q_2 \times 3600/\mathrm{RR}$, that is, $+13.1$ K cm^{-1} (-6 K cm^{-1}).

The present results can be directly evaluated against numerous previous estimates performed at larger scales using radiosondes or modeling, which are presented on an hourly or daily basis. To simplify comparison with those of the present paper, results of other studies will be presented as normalized moisture loss (production) Q_{2N} (K cm^{-1}). These estimates apply to various regions of the world, that is, oceans, coastal, and continental areas.

For instance, Johnson and Young (1983) quantify Q_2 from sounding data on ships during the MONEX experiment in the South China Sea. These estimations rely upon direct calculations and data interpolation in time and space. The Q_2 profiles calculated for seven mesoscale anvils show a great variability. The composite profile of Q_2 derived from these seven cases shows there is drying (by condensation and deposition) at altitudes higher than 5 km and moistening (by evaporation and melting) below. Maximum normalized moistening occurs at 2 km and is about -10.8 K cm^{-1} while maximum drying is about $+8.3$ K cm^{-1}. Other studies (e.g., Yanai et al. 1973) in which convective areas are taken into account in order to consider the whole system show very different results; that is, there is drying throughout the troposphere (Q_{2N} profiles are positive with values about $+4$ K cm^{-1} within Marshall Islands disturbances). Frank et al. (1996) also show convective-type (i.e., positive) profiles for Q_2 from the rawinsonde budget analyses during the 120 days of the TOGA COARE intensive observation period. A stratiform-type profile is not really observed in this study; Q_{2N} values are $+3.4$ K cm^{-1} within the intensive flux array (IFA), $+3.2$ K cm^{-1} within the outer soundings array (OSA), and $+2.4$ K cm^{-1} within the large-scale array (LSA), and they become smaller as far as the sampled area increases (see their Fig. 1).

Yang and Smith (2000) study is done within the IFA of TOGA COARE (see their Fig. 1). This paper shows slightly different results from combined TRMM Special Sensor Microwave Imager (SSM/I) and radiosonde analysis on TOGA COARE systems; that is, Q_{2N} is about $+3$ K cm^{-1} for convective systems throughout the troposphere, has a -2.5 K cm^{-1} minimal value at 2.5-km altitude, and has a $+1$ K cm^{-1} maximum value at 7-km altitude, within stratiform systems.

In their comparative study of AMEX and GATE cloud clusters, Frank and Mc Bride (1989) also show

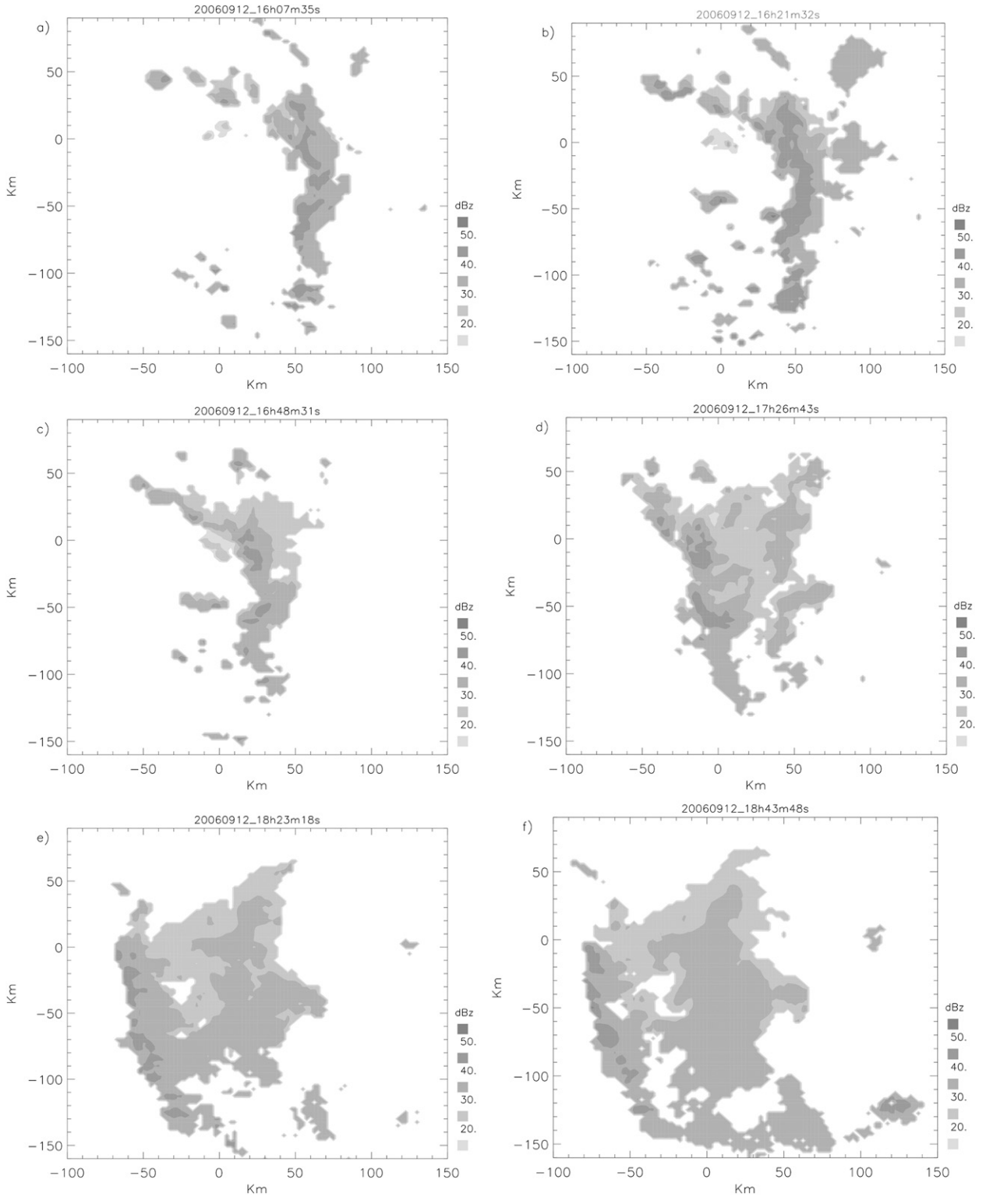

FIG. 10. Time evolution of horizontal radar reflectivity at (a) 1607, (b) 1621, (c) 1648, (d) 1728, (e) 1823, and (f) 1843 UTC 12 Sep 2006.

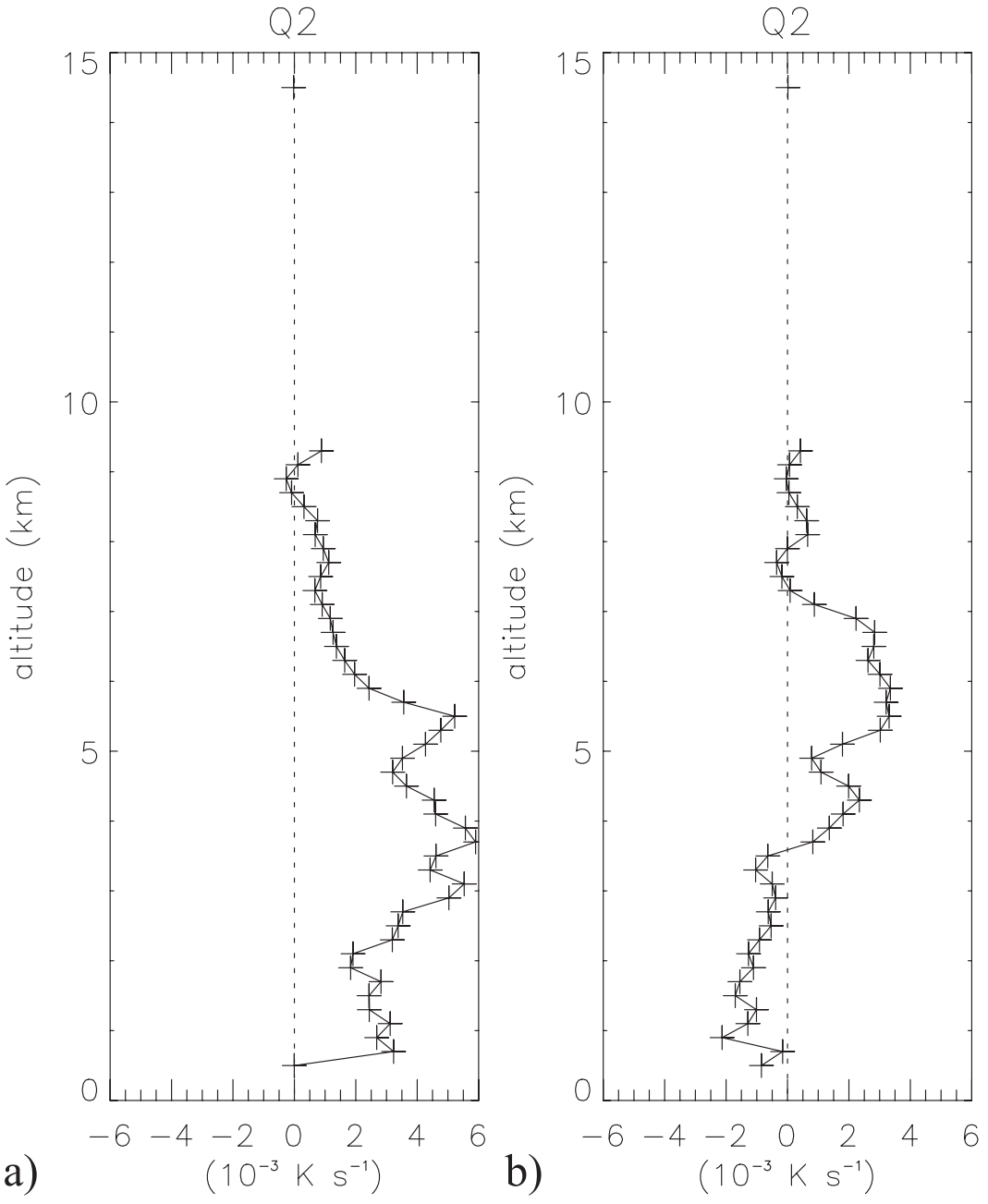

FIG. 11. The Q_2 profile (abscissa, 10^{-3} K s^{-1}) as a function of altitude (ordinate, km) at (a) 1720 and (b) 1733 UTC 12 Sep 2006.

positive profiles of Q_2 typical of convection, except in the last stage (decaying) of cloud clusters where Q_2 exhibits a negative profile below 900 mb. The Q_{2N} calculated on AMEX is reported in Yang and Smith (2000) as +4.5 K cm^{-1} for convective systems.

Johnson (1984) proposes partitioning Q_2 into components representing the contributions from cumulus clouds and mesoscale anvils, respectively, using an estimation of the fraction of the total rainfall produced by mesoscale anvil systems. The method is then applied to Q_2 profiles from various experiments and to a composite profile built from them. The results are here again similar: the convective profiles are positive, while the mesoscale components are again positive above the 0°C isotherm level, and negative below. Johnson (1984) shows that the vertical profile of Q_2 is a consequence of the drying–moistening from mesoscale anvils and cumulus cloud. Mesoscale anvils moisten the atmosphere below 5-km

altitude and dry upper levels. Cumulus clouds dry the total atmospheric column. Peaks of drying associated with each of these entities occur at well-separated altitudes. These altitudes correspond to the maximum removal of water vapor by net condensation for each cloud system, at the upper level for stratiform anvils and at the low level for cumulus clouds. This generally leads to a double-peak structure of drying depending on the relative contribution of each component.

Shige et al. (2008) have derived Q_2 profiles over six oceanic basins, using the spectral latent heating (SLH) algorithm for the TRMM PR. Here again, Q_2 profiles are in agreement with previous studies, that is, convective profiles show drying throughout the troposphere, and stratiform profiles exhibit moistening below 5 km and drying above. However, normalization could not be precisely performed in the absence of rain-rate data. Assuming 10 mm h^{-1} for the mean rain rate, maximal Q_{2N} loss would be between +1.5 and +3 K cm^{-1} within convection. For stratiform rain, Q_{2N} loss lies between +0.2 and +3 K cm^{-1} above 5 km, and Q_{2N} production lies between −0.2 and −1.6 K cm^{-1} above 5 km.

Results of Cifelli and Rutledge (1998) on north Australian MCSs appear similar to those realized in other regions in convective areas with positive Q_2 (drying) throughout the troposphere, while stratiform regions seem to play a much less important role than in other studies. Within convection, normalized mean Q_{2N} profiles exhibit maxima between +4 and +8 K cm^{-1} during monsoon or break regimes, respectively. Stratiform Q_{2N} profiles exhibit moisture production below 8 km, with maxima from about −4 to −5 K cm^{-1}.

The work by Schumacher et al. (2008) aimed at evaluating the role of specific cloud types in Q_1 and Q_2 budgets during KWAJEX over Marshall Islands (Kwajalein Island). It shows that cumulonimbus induce Q_{2N} profiles with maxima between +2.2 and +8 K cm^{-1}, while stratus and/or cumulus fractus of bad weather induce Q_{2N} profiles with maxima between 5.5 and 7 K cm^{-1}.

Johnson et al. (2010) studied the diurnal cycle of convection in northwest Mexico during NAME between the Gulf of California and the Sierra Madre Occidental, using a special sounding network including pibal data (winds as a function of height) and the S-band dual-polarization Doppler radar (S-Pol). The Q_{2N} profiles exhibit values between −7.5 and +7.5 K cm^{-1} using a mean rain rate of about 0.8 cm day^{-1} for Q_2 normalization.

Present results also can be compared to other results obtained by modeling using either 2D or 3D numerical models.

For instance, Tao et al. (1993) calculate Q_2 budgets by means of a 2D model on a midlatitude squall line observed during the Preliminary Regional Experiment for STORM Central (PRE-STORM) and on a tropical squall line observed during the Equatorial Mesoscale Experiment (EMEX) between Australia and New Guinea. The Q_2 profiles for the PRE-STORM convective region exhibit loss over the whole troposphere, while the anvil profiles exhibit moisture production between 850 and 650 hPa, and moisture loss below 850 and above 650 hPa. Because the mean rain rate is about 1.1 mm h^{-1}, the Q_{2N} maximal loss is +12.7 K cm^{-1} within convection and the Q_{2N} maximal production and loss are −7.7 K cm^{-1} and +3.6 K cm^{-1}, respectively, within anvils. Similarly, with a mean rain rate of about 1.2 mm h^{-1} during EMEX, the Q_{2N} profiles exhibit moisture loss throughout the troposphere in the convective regions, and experience production between 750 and 925 hPa, and loss elsewhere in anvil regions. Maximal Q_{2N} loss is +11.7 K cm^{-1} within convection. Maximum Q_{2N} production and loss are −3.3 and +4.2 K cm^{-1}, respectively, within anvils. These results appear rather strong, but this is probably due to the small value of the mean rain rates that are used as normalization factor.

Lafore et al. (1988) quantify Q_2 by modeling a squall line observed on 23–24 June 1981 during COPT 81 and observe Q_2 loss throughout the troposphere (except at about 500–450 mb) that is typical of convective areas. The main maximum normalized loss Q_{2N} is +7.4 K cm^{-1}.

Finally, the present results can be compared with those performed at the mesoscale and convective scale, that is, at the same scales as the present study, using 3D wind and microphysics fields retrieved from dual-beam Doppler measurements through elaborated retrieval methods.

For instance, Chong and Hauser (1990) have quantified moisture budgets for a squall line observed on 22 June 1981 during COPT 81, from the kinematics provided by Doppler radar (Chong et al. 1987), and the thermodynamics and microphysics diagnosed from a stationary model (Chong and Hauser 1989). Total Q_2 is shown to be positive above 2 km. Partitioning into the convective scale and mesoscale components of Q_2 shows that the convective-scale component is positive throughout the troposphere, while the mesoscale component is negative below 4 km, about 0°C isotherm.

A more detailed comparison can be done between the present study and that of Chong and Hauser (1990), which was performed at similar scales. Their Q_2 partitioning into two components (see their Fig. 7) shows that the convective component contribution is important at lower altitude and decreases the altitude of the total (convective + stratiform) peak, which depends on the respective contribution of convective and stratiform components. Using their total rain rate of 17.8 cm day^{-1}, their total Q_{2N} peak is about +10–11 K cm^{-1} close to the present mean

normalized estimate. Their convective Q_{2N} maximum (moisture loss) is about $+6$ K cm^{-1} at 5.5-km altitude, while their stratiform Q_{2N} maximum is about 5 K cm^{-1} at 7-km altitude, and their stratiform Q_{2N} minimum is about -3 K cm^{-1} (moisture production) at 2-km altitude.

In summary from these comparisons the following main conclusions can be drawn:

1) The Q_2 profiles obtained on three AMMA squall lines oscillate between two types. The first one exhibits moisture production at low levels below 2–3 km and moisture loss above and up to 7–10 km; this is characteristic of mixed convective–stratiform situations in which convective cores are surrounded by stratiform reflectivities. The second type of Q_2 profiles exhibits loss over a large portion of the troposphere. This signs the effect of upward vertical velocities associated with convective areas. They are in reasonable agreement with results of other studies performed at larger scales in mainly stratiform squall-line anvils.
2) The Q_{2N} values about -6 and $+13$ K cm^{-1} obtained in the present study are close to those from studies focusing on precipitating areas (Chong and Hauser 1990; Tao et al. 1993), and are somewhat higher than those focusing on whole systems, which include precipitation-free areas. For studies focusing on whole systems, the differences on space scales (30–500 km) and time scales (2–3 h, 1 day) affect both Q_2 and the rain rate in the same way, so that Q_{2N} should be comparable if both domains contained precipitation. However, the greater domain is partly free from precipitation; thus, in that case, the mean vertical velocity W is smaller than the one that would be obtained in a domain totally covered with precipitation. Because Q_2 (and Q_{2N}) are proportional to W in first approximation, this could partly explain the observed difference. Moreover, as suggested by Chong and Hauser (1990), the residual differences between cases studied during a short and long time may come from the fact that averaging on a longer time period may include several stages of development of the systems. Finally, an additional difference could result from the oceanic or continental character of the precipitating systems.
3) The other studies that include strong convective-scale precipitation find profiles that are positive throughout the troposphere, that is, that dry the environment. This could be observed by radar on the 30-km profiles whenever the most active parts of the squall lines were intercepted by the radar.
4) The present profiles suggest the contribution of a notable convective component thus confirming the mixed convective–stratiform character of the present AMMA cases.

5. Conclusions and perspectives

This study shows that Q_2 calculation within convective systems is possible from Doppler radar observations by processing the wind and reflectivity data. For this purpose the radar winds are analyzed using the robust classical VAD analysis, and afterward a specific method to process the radar reflectivity in order to derive precipitation mixing ratio and its derivatives was developed. The obtained Q_2 profiles for the three studied cases are in agreement with profiles obtained at a larger scale and are comparable with those obtained at mesoscale.

Normalized Q_{2N} profiles obtained by radar present characteristics in agreement with those observed on mesoscale anvils. Moisture production is located at lower levels, consistent with evaporation, while midlevel moisture loss is consistent with condensation and deposition. Normalized Q_{2N} values are somewhat higher than most of those deduced at larger scales, but are consistent with those obtained within systems. A part of this residual difference can be explained by the fact that present Q_2 values are representative of about 1 or 2 h of measurements and cannot be extrapolated to 24 h, except if constant rain rate is assumed during 24 h.

These Q_2 profiles present characteristics that are observed at mesoscale within mixed convective–stratiform situations, in which convective cores are surrounded by stratiform area.

The originality and the main interest of the present approach, when compared to previous studies, rely on the fact radar data are used and that the study is based upon a relatively low-cost analysis, allowing for systematic application on large datasets in the future and allowing statistical studies.

Thus, the first perspective of the present work is a systematic application of the method to the ensemble of convective systems observed during the AMMA campaign. A second perspective that corresponds to a work presently in progress is to apply a similar method to Q_1, although a method totally relying on the radar data needs additional hypotheses in the case of Q_1.

Acknowledgments. Based on a French initiative, AMMA was built by an international scientific group and is currently funded by a large number of agencies from France, the United Kingdom, the United States, and Africa. It has been the beneficiary of a major financial contribution from the European Community's

Sixth Framework Research Programme. Detailed information on scientific coordination and funding is available on the AMMA International web site (http://www.ammainternational.org).

REFERENCES

Bréger, G., 1977: Etude par radar Doppler de mouvements atmosphériques au voisinage d'un front froid (in French). Thèse de 3ème cycle, Université Pierre et Marie Curie-Paris VI, 108 pp.

Browning, K. A., and R. Wexler, 1968: The determination of kinematic properties of a wind field using Doppler radar. *J. Appl. Meteor.,* **7,** 105–113.

Chong, M., and D. Hauser, 1989: A tropical squall line observed during the COPT 81 experiment in West Africa. Part II: Water budget. *Mon. Wea. Rev.,* **117,** 728–744.

——, and ——, 1990: A tropical squall line observed during the COPT 81 experiment in West Africa. Part III: Heat and moisture budgets. *Mon. Wea. Rev.,* **118,** 1696–1706.

——, P. Amayenc, G. Scialom, and J. Testud, 1987: A tropical squall line observed during the COPT 81 experiment in West Africa. Part I: Kinematic structure inferred from dual-Doppler radar data. *Mon. Wea. Rev.,* **115,** 670–694.

Chumchean, S., A. Seed, and A. Sharma, 2004: Application of scaling in radar reflectivity for correcting range-dependent bias in climatological radar rainfall estimates. *J. Atmos. Oceanic Technol.,* **21,** 1545–1556.

Cifelli, R., and S. A. Rutledge, 1998: Vertical motions, diabatic heating, and rainfall characteristics in North Australia convective systems. *Quart. J. Roy. Meteor. Soc.,* **124,** 1133–1162.

Evaristo, R., G. Scialom, N. Viltard, and Y. Lemaître, 2010: Polarimetric signatures and hydrometeor classification of West African squall line. *Quart. J. Roy. Meteor. Soc.,* **136** (S1), 272–288.

Frank, W. M., and J. L. Mc Bride, 1989: Vertical distribution of heating in AMEX and GATE cloud clusters. *J. Atmos. Sci.,* **46,** 3464–3478.

——, H.-J. Wang, and J. L. Mc Bride, 1996: Rawinsonde budget analyses during the TOGA COARE IOP. *J. Atmos. Sci.,* **53,** 1761–1780.

Gallus, W. A., and R. H. Johnson, 1991: Heat and moisture budgets of an intense midlatitude squall line. *J. Atmos. Sci.,* **48,** 122–146.

Hauser, D., and P. Amayenc, 1986: Retrieval of cloud water and water vapor contents from Doppler radar data in a tropical squall line. *J. Atmos. Sci.,* **43,** 823–838.

Heymsfield, G. M., and S. Schotz, 1985: Structure and evolution of a severe squall line over Oklahoma. *Mon. Wea. Rev.,* **113,** 1563–1589.

Higgins, W., and Coauthors, 2006: The NAME 2004 field campaign field and modeling strategy. *Bull. Amer. Meteor. Soc.,* **87,** 79–94.

Houze, R. A., 1977: Structure and dynamics of a tropical squall-line system. *Mon. Wea. Rev.,* **105,** 1540–1567.

——, 1982: Cloud clusters and large-scale vertical motions in the tropics. *J. Meteor. Soc. Japan,* **60,** 396–409.

Hung, C.-W., and M. Yanai, 2004: Factors contributing to the onset of the Australian summer monsoon. *Quart. J. Roy. Meteor. Soc.,* **130,** 739–758.

Johnson, R. H., 1984: Partitioning tropical heat and moisture budgets into cumulus and mesoscale components: Implications for cumulus parameterization. *Mon. Wea. Rev.,* **112,** 1590–1601.

——, and G. S. Young, 1983: Heat and moisture budgets of tropical mesoscale anvil clouds. *J. Atmos. Sci.,* **40,** 2138–2147.

——, and P. E. Ciesielski, 2002: Characteristics of the 1988 summer monsoon onset over the northern South China Sea. *J. Meteor. Soc. Japan,* **80,** 561–578.

——, ——, T. S. L'Ecuyer, and A. J. Newman, 2010: Diurnal cycle of convection during the 2004 North American Monsoon Experiment. *J. Climate,* **23,** 1060–1078.

Lafore, J.-P., J.-L. Redelsperger, and G. Jaubert, 1988: Comparison between a three-dimensional simulation and Doppler radar data of a tropical squall line: Transports of mass, momentum, heat, and moisture. *J. Atmos. Sci.,* **45,** 3483–3500.

Le Bouar, E., J. Testud, and T. D. Keenan, 2001: Validation of the rain profiling algorithm ''ZPHI'' from the C-band polarimetric weather radar in Darwin. *J. Atmos. Oceanic Technol.,* **18,** 1819–1837.

Lemaître, Y., 1982: Etude dynamique et thermodynamique de lignes de grains tropicales observées à Korhogo pendant l'expérience COPT 79. *J. Rech. Atmos.,* **16,** 47–69.

——, and J. Testud, 1986: Observation and modelling of tropical squall lines observed during the 'COPT 79' experiment. *Ann. Geophys.,* **4B,** 21–36.

Li, W., D. Wang, T. Lei, and H. Wang, 2009: Convective and stratiform rainfall and heating associated with the summer monsoon over the South China Sea based on TRMM data. *Theor. Appl. Climatol.,* **95,** 157–163.

Lin, X., and R. H. Johnson, 1994: Heat and moisture budgets and circulation characteristics of a frontal squall line. *J. Atmos. Sci.,* **51,** 1661–1681.

Maddox, R. A., 1980: Mesoscale convective complexes. *Bull. Amer. Meteor. Soc.,* **61,** 1374–1387.

——, 1983: Large-scale meteorological conditions associated with midlatitude, mesoscale convective complexes. *Mon. Wea. Rev.,* **111,** 1475–1493.

Magagi, R., and A. P. Barros, 2004: Estimation of latent heating of rainfall during the onset of the Indian monsoon using TRMM PR and radiosonde data. *J. Appl. Meteor.,* **43,** 328–349.

Marécal, V., 1992: Etude microphysique et thermodynamique de bandes de précipitations frontales à partir d'observations par radars Doppler (in French). Ph.D. thesis, Université Paris 7, 284 pp.

Matejka, T. J., and R. C. Srivastava, 1981: Doppler radar study of a region of widespread precipitation trailing a mid-latitude squall line. Preprints, *20th Conf. on Radar Meteorology,* Boston, MA, Amer. Meteor. Soc., 353–357.

Raymond, J. D., and Coauthors, 2004: EPIC2001 and the coupled ocean–atmosphere system of the tropical east Pacific. *Bull. Amer. Meteor. Soc.,* **85,** 1341–1354.

Redelsperger, J.-L., C. D. Thorncroft, A. Diedhiou, T. Lebel, D. J. Parker, and J. Polcher, 2006: African monsoon multidisciplinary analysis: An international research project and field campaign. *Bull. Amer. Meteor. Soc.,* **87,** 1739–1746.

Schumacher, C., P. E. Cieselski, and M. H. Zhang, 2008: Tropical cloud heating profiles analysis from KWAJEX. *Mon. Wea. Rev.,* **136,** 4289–4300.

Scialom, G., J. Faroux, M. Giraud, R. Ney, R. Evaristo, Y. Lemaître, and N. Viltard, 2009: RONSARD radar: Implementation of dual polarization on a C-band Doppler weather radar. *IEEE Geosci. Remote Sens. Lett.,* **6,** 132–136.

Shige, S., Y. N. Takayabu, W.-K. Tao, and D. E. Johnson, 2004: Spectral retrieval of latent heating profiles from TRMM PR data. Part I: Development of a model-based algorithm. *J. Appl. Meteor.,* **43,** 1095–1113.

——, ——, ——, and C.-L. Shie, 2007: Spectral retrieval of latent heating profiles from TRMM PR data. Part II: Algorithm improvement and heating estimates over tropical ocean regions. *J. Appl. Meteor. Climatol.,* **46,** 1098–1124.

——, ——, and ——, 2008: Spectral retrieval of latent heating profiles from TRMM PR data. Part III: Estimating apparent moisture sink profiles over tropical oceans. *J. Appl. Meteor. Climatol.,* **47,** 620–640.

——, ——, S. Kida, W.-K. Tao, X. Zeng, C. Yokoyama, and T. L'Ecuyer, 2009: Spectral retrieval of latent heating profiles from TRMM PR data. Part IV: Comparisons of lookup tables from two- and three-dimensional cloud-resolving model simulations. *J. Climate,* **22,** 5577–5594.

Silva Dias, M. A. F., and Coauthors, 2002: Cloud and rain processes in a biosphere-atmosphere interaction context in the Amazon Region. *J. Geophys. Res.,* **107,** 8072, doi:10.1029/2001JD000335.

Simpson, J., R. F. Adler, and G. R. North, 1988: A proposed Tropical Rainfall Measuring Mission (TRMM) satellite. *Bull. Amer. Meteor. Soc.,* **69,** 278–294.

Smull, B. F., and R. A. Houze, 1985: A midlatitude squall line with a trailing region of stratiform rain: Radar and satellite observations. *Mon. Wea. Rev.,* **113,** 117–133.

Tao, W. K., J. Simpson, C.-H. Sui, B. Ferrier, S. Lang, J. Scala, M.-D. Chou, and K. Pickering, 1993: Heating, moisture and water budgets of tropical and midlatitude squall lines: Comparisons and sensitivity to longwave radiation. *J. Atmos. Sci.,* **50,** 673–690.

Testud, J., E. Le Bouar, E. Obligis, and M. Ali-Mehenni, 2000: The rain profiling algorithm applied to polarimetric weather radar. *J. Atmos. Oceanic Technol.,* **17,** 332–356.

Yanai, M., S. Esbensen, and J.-H. Chu, 1973: Determination of bulk properties of tropical cloud clusters from large-scale heat and moisture budgets. *J. Atmos. Sci.,* **30,** 611–627.

Yang, S., and E. A. Smith, 2000: Vertical structure and transient behavior of convective–stratiform heating in TOGA-COARE from combined satellite-sounding analysis. *J. Appl. Meteor.,* **39,** 1491–1513.

Yuter, S. E., and R. A. Houze, 2000: The 1997 Pan American Climate Studies Tropical Eastern Pacific Process Studies. Part I: ITCZ region. *Bull. Amer. Meteor. Soc.,* **81,** 451–481.

Zipser, E. J., 1977: Mesoscale and convective-scale downdrafts as distinct components of squall-line structure. *Mon. Wea. Rev.,* **105,** 1568–1589.

——, R. J. Meitin, and M. A. Lemone, 1981: Mesoscale motions fields associated with a slowly moving GATE convective band. *J. Atmos. Sci.,* **38,** 1725–1750.

——, and Coauthors, 2009: The Saharan air layer and the fate of African easterly waves. NASA's AMMA field study of tropical cyclogenesis. *Bull. Amer. Meteor. Soc.,* **90,** 1137–1156.